arXiv seminar
#GAEP 0927-1003 1-67

百瀬宗武（茨城大）

以下の4本を紹介 (No.33と32は密接に関連する)

- No.08: Volatile composition of the HD 169142 disk and its embedded planet
- No.33: Discovery of interstellar 1-cyanopyrene: a four-ring polycyclic aromatic hydrocarbon in TMC-1
- No.32: Detections of interstellar 2-cyanopyrene and 4-cyanopyrene in TMC-1
- No.51: JWST imaging of edge-on protoplanetary disks III. Drastic morphological transformation across the mid-infrared in Oph163131

Volatile composition of the HD 169142 disk and its embedded planet

Luke Keyte, Mihkel Kama, Alice S. Booth, Charles J. Law, Margot Leemker

ABSTRACT

The composition of a planet's atmosphere is intricately linked to the chemical makeup of the protoplanetary disk in which it formed. Determining the elemental abundances from key volatiles within disks is therefore essential for establishing connections between the composition of disks and planets. The disk around the Herbig Ae star HD 169142 is a compelling target for such a study due to its molecule-rich nature and the presence of a newly-forming planet between two prominent dust rings. In this work, we probe the chemistry of the HD 169142 disk at small spatial scales, drawing links between the composition of the disk and the planet-accreted gas. Using thermochemical models and archival data, we constrain the elemental abundances of volatile carbon, oxygen, and sulfur. Carbon and oxygen are only moderately depleted from the gas phase relative to their interstellar abundances, with the inner ~60 au appearing enriched in volatile oxygen. The C/O ratio is approximately solar within the inner disk (~0.5) and rises above this in the outer disk (>0.5), as expected across the H_2O snowline. The gas-phase sulfur abundance is depleted by a factor of ~1000, consistent with a number of other protoplanetary disks. Interestingly, the observed SiS emission near the HD 169142 b protoplanet vastly exceeds chemical model predictions, supporting previous hypotheses suggesting its origin in shocked gas or a localised outflow. We contextualise our findings in terms of the potential atmospheric composition of the embedded planet, and highlight the utility of sulfur-bearing molecules as probes of protoplanetary disk chemistry.

Key words: protoplanetary disks – exoplanets – planets and satellites: formation – submillimetre: planetary systems

Volatile composition of the HD 169142 disk and its embedded planet

Luke Keyte, Mihkel Kama, Alice S. Booth, Charles J. Law, Margot Leemker

- 惑星存在が示唆されている HD 169142 円盤に対するガスアーカイブデータを包括的に解析
- 円盤物理モデル + 化学反応計算に基づき，ガス動径分布を再現するガス中の元素存在比 C/O や S存在比を議論
- CS/SO 比から，C/Oが変化が水Snowlineの内側(~0.5)と外側(>0.5)で違う
- 惑星存在が議論されている位置でのSiSのenhanceはこれまでの化学モデルでは説明できない
- 惑星大気の初期化学組成への示唆を議論（していたがここでは省略）

背景，及びHD169142のダスト円盤

- 円盤リングギャップは惑星の兆候だが，惑星なしの起源も考えられる
- 円盤のvolatile elementsの分布・存在量と惑星大気の間に関係は複雑
  - C/O分布（C_2Hのモデリングなど）
  - Snowlineが鍵? 水氷の落下やダスト集積
  - 他の指標: C/N, N/O, S/N… Sは特に要注目
- HD169142：惑星存在が示唆，S-speciesの検出が豊富，良いターゲット

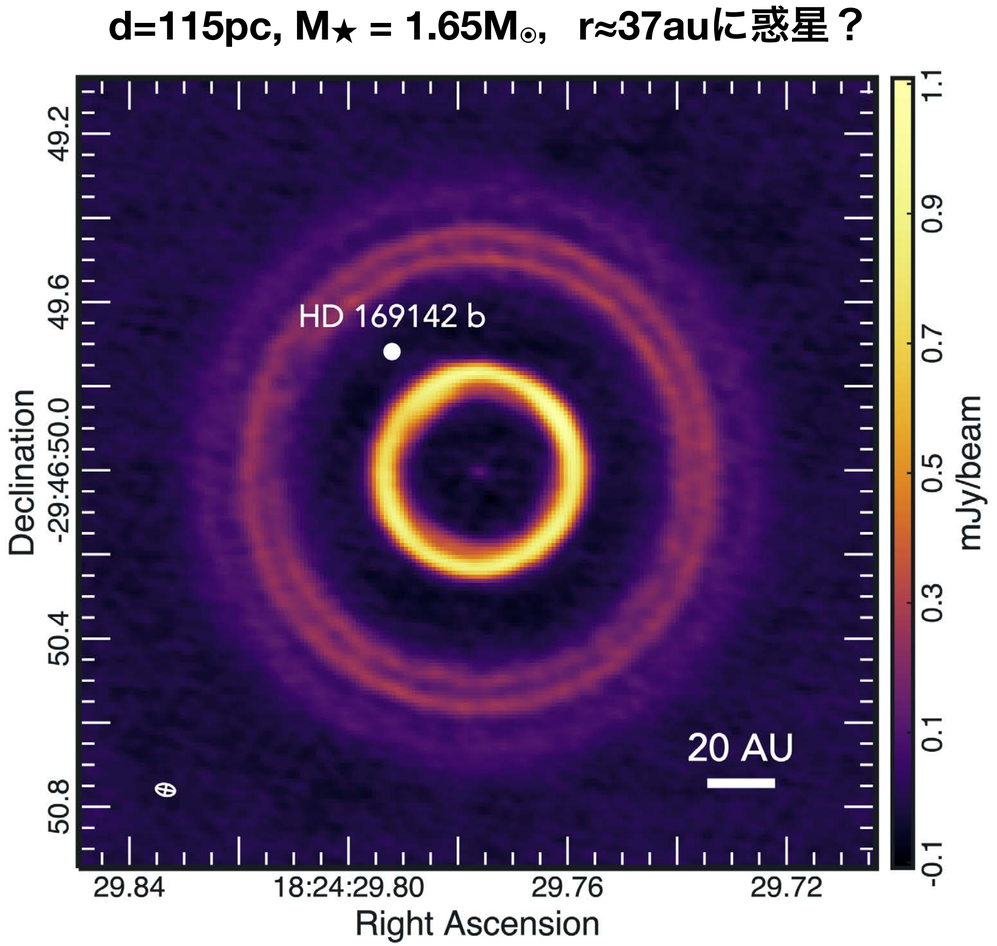

Figure 1. ALMA 1.3mm continuum observation of the HD 169142 system (Pérez et al. 2019), including the inferred location of the HD 169142 b protoplanet (Hammond et al. 2023). The synthesized beam is indicated by the white ellipse in the lower left.

使用するデータセット

Table A1: Summary of archival observational data used in this study.

Species	Transition	ν (GHz) [a]	Beam Size	A_{ul} (s^{-1}) [a]	E_{up} (K) [a]	Project [b]	PI	Reference
			ALMA 12m array					
CONT	0.45 mm	670.583700	0.04"×0.04" (-72°)	-	-	2017.1.00727.S	J. Szulágyi	Leemker et al. (2022)
CONT	0.89 mm	331.000000	0.05"×0.03" (80°)	-	-	2012.1.00799.S	M. Honda	Law et al. (2023)
CONT	1.3 mm	225.000000	0.04"×0.02" (73°)	-	-	2016.1.00344.S	S. Perez	Garg et al. (2022)
CO	$J = 2 - 1$	230.538000	0.05"×0.03" (80°)	6.857×10^{-7}	16.6	2016.1.00344.S	S. Perez	Garg et al. (2022)
CO	$J = 3 - 2$	345.795990	0.11"×0.09" (74°)	2.476×10^{-6}	33.2	2012.1.00799.S / 2015.1.00806.S	M. Honda / J.Pineda	Law et al. (2023)
^{13}CO	$J = 2 - 1$	220.398684	0.05"×0.04" (78°)	6.038×10^{-7}	15.9	2016.1.00344.S	S. Perez	Garg et al. (2022)
^{13}CO	$J = 3 - 2$	330.587965	0.12"×0.09" (75°)	2.181×10^{-6}	31.7	2012.1.00799.S / 2015.1.00806.S	M. Honda / J.Pineda	Law et al. (2023)
^{13}CO	$J = 6 - 5$	661.067277	0.06"×0.05" (86°)	1.868×10^{-5}	111.1	2017.1.00727.S	J. Szulágyi	Leemker et al. (2022)
C^{18}O	$J = 2 - 1$	219.560354	0.07"×0.06" (-46°)	6.011×10^{-7}	15.8	2016.1.00344.S	S.Perez	Garg et al. (2022)
[CI]	$^3P_1 - ^3P_0$	492.160651	1.01"×0.51" (81°)	7.880×10^{-8}	23.6	2016.1.00346.S	T. Tsukagoshi	Booth et al. (2023a)
CS	$J = 10 - 9$	489.750921	0.94"×0.40" (83°)	2.496×10^{-3}	129.3	2016.1.00346.S	T. Tsukagoshi	Booth et al. (2023a)
^{13}CS	$J = 6 - 5$	277.455405	0.73"×0.46" (89°)	4.399×10^{-4}	46.6	2018.1.01237.S	E. Macias	Booth et al. (2023a)
SO	$J = 8_8 - 7_7$	344.310612	0.19"×0.14" (89°)	5.186×10^{-4}	87.5	2012.1.00799.S / 2015.1.00806.S	M. Honda / J.Pineda	Law et al. (2023)
H_2CS	$J = 8_{1,7} - 7_{1,6}$	278.887661	0.73"×0.46" (89°)	3.181×10^{-4}	73.4	2018.1.01237.S	E. Macias	Booth et al. (2023a)
SiS	$J = 19 - 18$	344.779481	0.19"×0.14" (84°)	6.996×10^{-4}	165.5	2012.1.00799.S	M. Honda	Law et al. (2023)
			Herschel/PACS					
HD	56μm	5331.56195	-	4.860×10^{-7}	384.6	DIGIT	N.J. Evans	Kama et al. (2020)
HD	112μm	2674.98609	-	5.440×10^{-8}	128.5	DIGIT	N.J. Evans	Kama et al. (2020)
[OI]	63μm	4747.77749	-	8.910×10^{-5}	227.7	GASPS	W.R.F. Dent	Meeus et al. (2012)
[OI]	146μm	2061.06909	-	1.750×10^{-5}	326.6	GASPS	W.R.F. Dent	Meeus et al. (2012)

[a] Line frequencies, Einstein A coefficients (A_{ul}), and upper energy levels (E_{up}) are taken from the Cologne Database for Molecular Spectroscopy (CDMS; Müller et al. 2001; Müller et al. 2005; Endres et al. 2016) and the Leiden Atomic and Molecular Database (LAMDA; Schöier et al. 2005)

[b] Observations listed with two project IDs combined both datasets

手法：円盤モデルとアーカイブデータを比較

1. 円盤構造を決める
   - ガス円盤は通常のpower-law with an exponential taper
   - ダスト連続波(SED及び高解像度イメージ）を再現するダスト円盤構造決める
   - HD 56umと112umの上限値からgas massの最大値を制限，ただ結局大した制約は得られず g/d = 100に固定。。。
2. 化学ネットワーク計算の詳細(DALIの拡張）
   - CO isotopologuesの同位体分別を引き起こす反応を含めた基本化学反応ネットワーク　＋ Sulfer 関連反応の大幅な拡張
   - 5Myr にわたって計算，分布を求める
3. ガス化学に関連したパラメータサーチ
   - $C^{18}O$の動径分布や[CI]や[OI]の放射を再現するようO/HやC/Hを振ってみる
   - CSやSOなどのデータ（特に両者の比の動径分布）を再現するSのガス存在比やC/O動径分布を探す

柱密度

$$\Sigma_{\rm gas} = \Sigma_{\rm c} \cdot \left(\frac{r}{R_c}\right)^{-\gamma} \exp\left[-\left(\frac{r}{R_c}\right)^{2-\gamma}\right]$$

スケールハイト

$$h(r) = h_c \left(\frac{r}{R_c}\right)^{\psi}$$

大きなダストと小さなダストに分けて鉛直構造を考える

$$\rho_{\rm dust,\ large} = \frac{f\Sigma_{\rm dust}}{\sqrt{2\pi} r \chi h} \exp\left[-\frac{1}{2}\left(\frac{\pi/2-\theta}{\chi h}\right)^2\right]$$

$$\rho_{\rm dust,\ small} = \frac{(1-f)\Sigma_{\rm dust}}{\sqrt{2\pi} r h} \exp\left[-\frac{1}{2}\left(\frac{\pi/2-\theta}{h}\right)^2\right]$$

ψ，h_c. Δg/d，χ，f を モデルグリッドから探索

Table B1. Fiducial HD 169142 disk model parameters.

Parameter	Description	Fiducial
$R_{\rm sub}$	Sublimation radius	0.2 au
$R_{\rm gap}$	Inner disk size	0.4 au
$R_{\rm gas.cav}$	Gas cavity inner radius	13 au
$R_{\rm cav}$	Dust cavity radius	21 au
$R_{\rm dust.gap.in}$	Dust gap inner radius	32 au
$R_{\rm gas.gap.in}$	Gas gap inner radius	32 au
$R_{\rm dust.gap.out}$	Dust gap outer radius	56 au
$R_{\rm gas.gap.out}$	Gas gap outer radius	56 au
$R_{\rm L.dust.out}$	Maximum radius of large dust grains	83 au
$R_{\rm out}$	Disk outer radius	180 au
R_c	Critical radius for surface density	100 au
$\delta_{\rm gas}$	Gas depletion factor inside $R_{\rm gas.cav}$	10^{-10}
$\delta_{\rm gas.cav.edge}$	Gas depletion factor between $R_{\rm gas.cav}$ - $R_{\rm cav}$	10^{-3}
$\delta_{\rm gas.ring}$	Gas depletion factor between $R_{\rm cav}$- $R_{\rm dust.gap.in}$	1.0
$\delta_{\rm L.dust}$	Large dust grain depletion factor inside $R_{\rm cav}$	10^{-10}
$\delta_{\rm S.dust}$	Small dust grain depletion factor inside $R_{\rm cav}$	10^{-10}
$\delta_{\rm L.dust.ring}$	Large dust grain depletion factor between $R_{\rm cav}$- $R_{\rm dust.gap.in}$	0.27
$\delta_{\rm S.dust.ring}$	Small dust grain depletion factor between $R_{\rm cav}$- $R_{\rm dust.gap.in}$	0.27
$\delta_{\rm L.dust.gap}$	Large dust grain depletion factor between $R_{\rm dust.gap.in}$ - $R_{\rm dust.gap.out}$	10^{-10}
$\delta_{\rm S.dust.gap}$	Small dust grain depletion factor between $R_{\rm dust.gap.in}$ - $R_{\rm dust.gap.out}$	10^{-2}
γ	Power law index of surface density profile	1.0
χ	Dust settling parameter	0.2
f	Large-to-small dust mixing parameter	0.85
Σ_c	$\Sigma_{\rm gas}$ at R_c	8.125 g cm^{-2}
h_c	Scale height at R_c	0.07 rad
ψ	Power law index of scale height	0.0
$\Delta_{\rm g/d}$	Gas-to-dust mass ratio	100
L_*	Stellar luminosity	10 $L_\odot$
T_*	Stellar temperature	8400 K
L_X	Stellar X-ray luminosity	7.94×10^{28} erg s^{-1}
T_X	X-ray plasma temperature	7.0×10^7 K
$\zeta_{\rm cr}$	Cosmic ray ionization rate	1.26×10^{-17} s^{-1}
$M_{\rm gas}$	Disk gas mass	2.83×10^{-2} $M_\odot$
$M_{\rm dust}$	Disk dust mass	1.11×10^{-4} $M_\odot$
$t_{\rm chem}$	Timescale for time-dependent chemistry	5 Myr

Model grid

Table B2. Fiducial HD 169142 disk model initial abundances and range of values covered by the model grid.

Species	Abundance (X/H)	Range
H	1.0	-
He	7.59×10^{-2}	-
C	1.00×10^{-4}	2×10^{-5} to 2×10^{-4}
O	1.00×10^{-4}	2×10^{-5} to 2×10^{-4}
N	2.14×10^{-5}	-
S	4.00×10^{-8}	1×10^{-12} to 1×10^{-5}
Mg	1.00×10^{-11}	-
Si	1.00×10^{-11}	-
Fe	1.00×10^{-11}	-

dustデータの再現

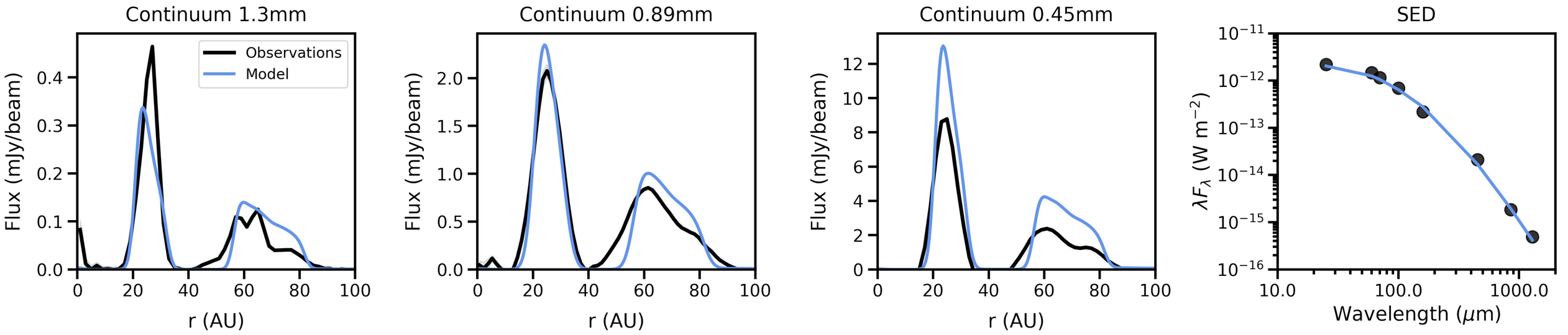

Figure B2. Continuum radial intensity profiles and spectral energy distribution (SED). Observations are shown in black and fiducial model in blue.

COデータの再現(1): C/Oを振ってみる

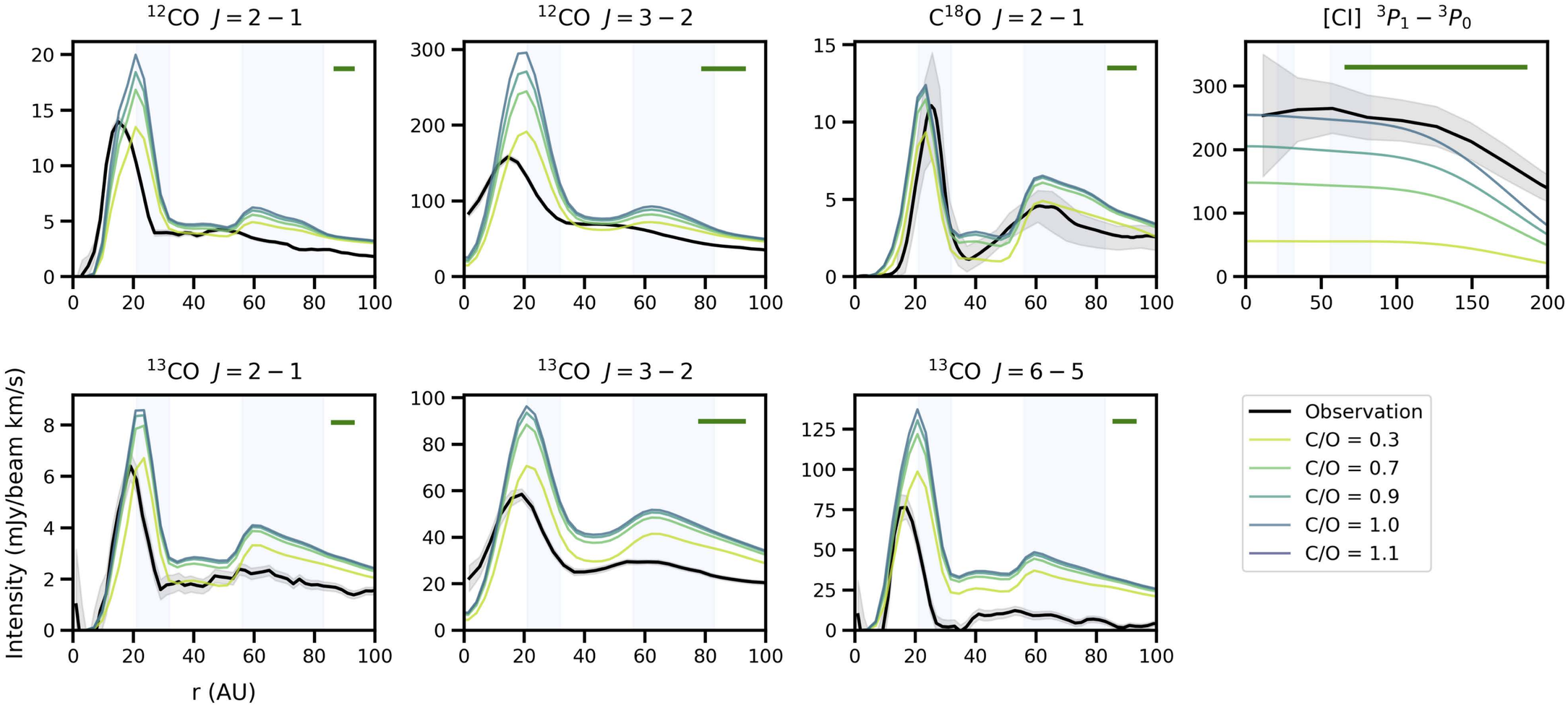

COデータの再現(2): C/O=1としてC/Hを振ってみる

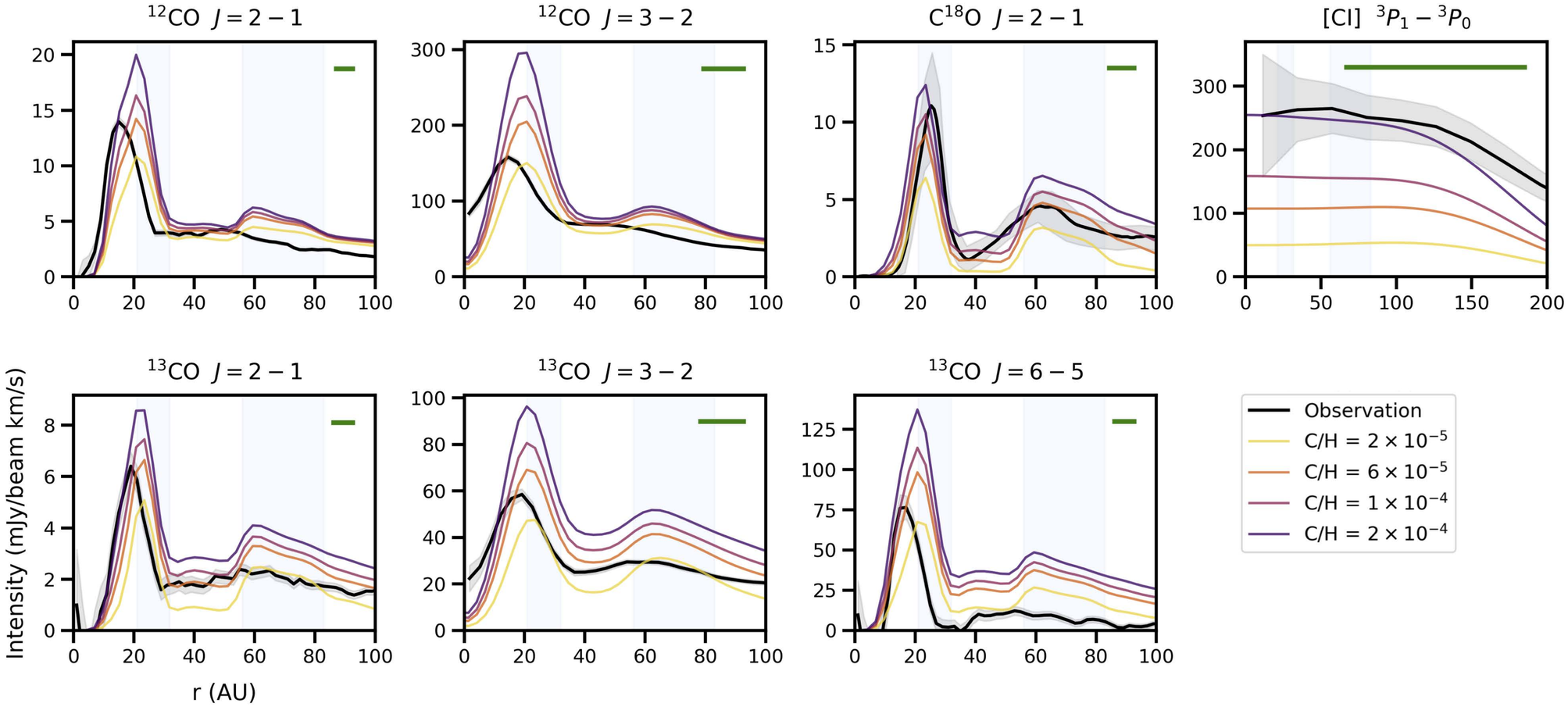

全部を満足するモデルはないが，C/O=1.0, C/H=1×10^{-4} として，C^{18}Oが合うようにGas depletion を議論：

過去の研究と異なり，inner ring (r=21-32au)ではさほどgas depletion なし(gas depletion factor = 1.0)

gap (32-56 au)では gas depletion factor = 0.02 (論文中であまりちゃんと説明していないので良くわからない)

CS, ^{13}CS, SO, H_2CSからS/Hを議論

S/H ~ 10^{-8}くらいに激しくdepleteしてないと，輝線強度の絶対値が再現できない

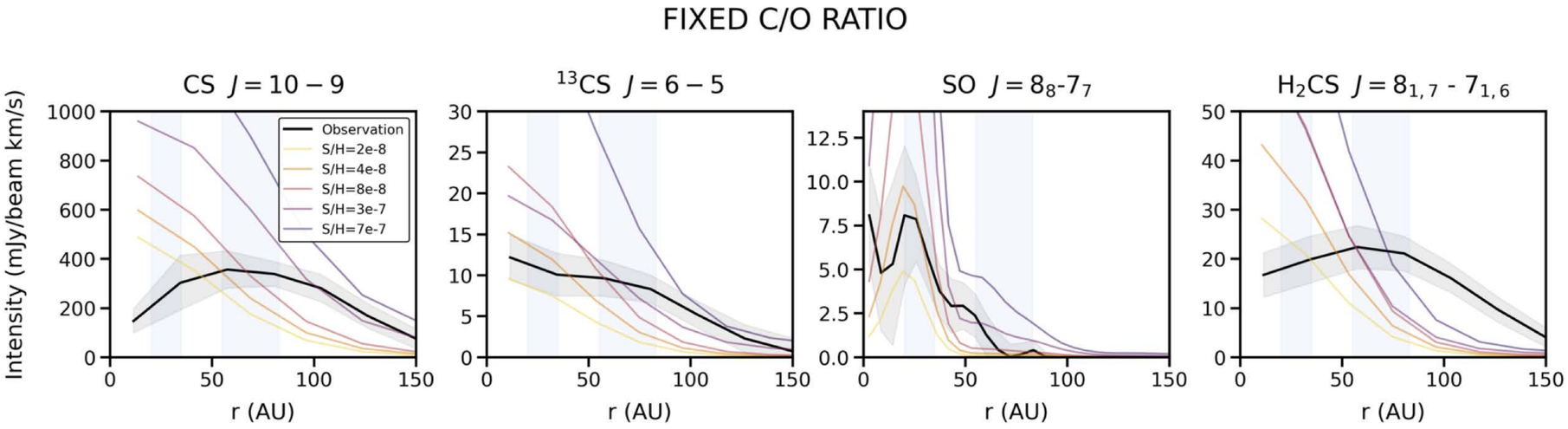

C/O に依存して CSとSOの変化の仕方が少し変わる

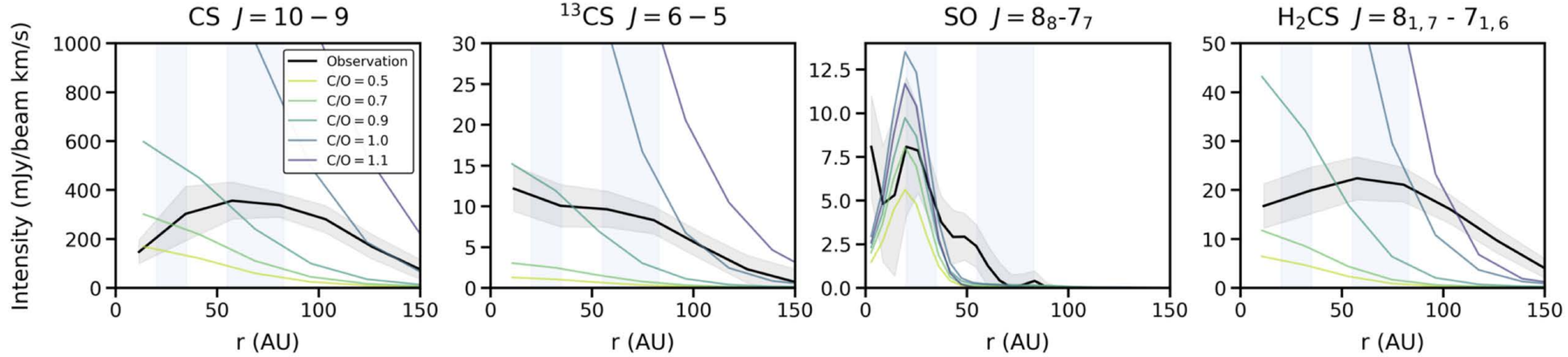

CS/SO比を再現するにはcomposite model

内側でC/O = 0.5, 外側でC/O>0.5が必要

Cが多ければCSは増える

Oが増えてもSOはさほど増えない(SO_2になる)

この点は先行研究でも指摘あり

(Semenov+ 2018; Le Gal+ 2021など)

水Snowlineの内外でC/Oは変化している

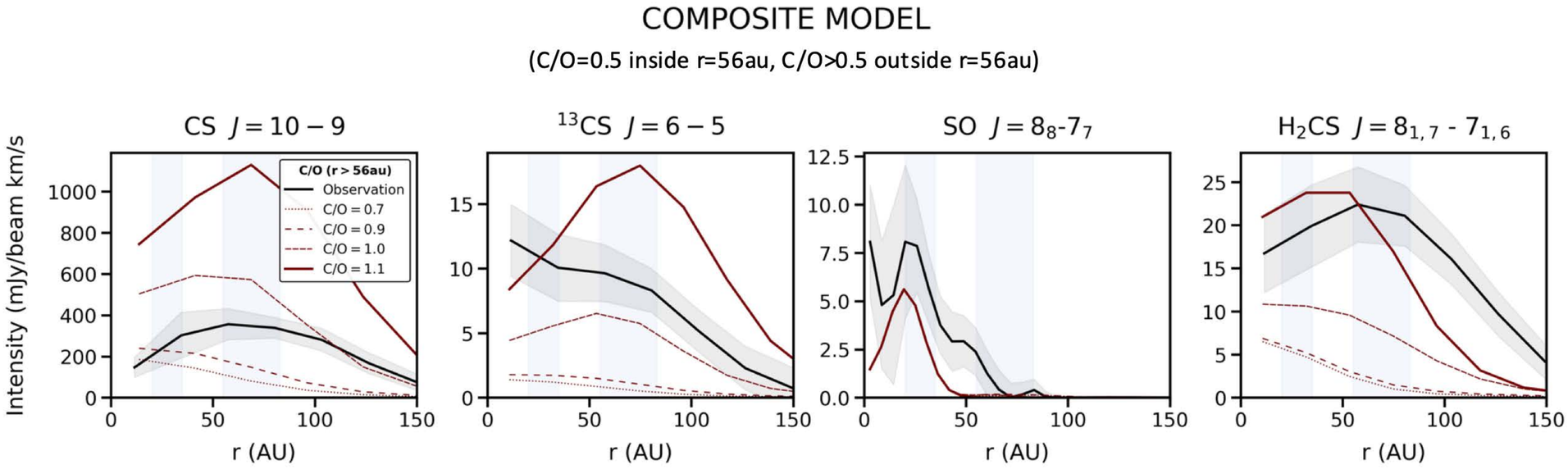

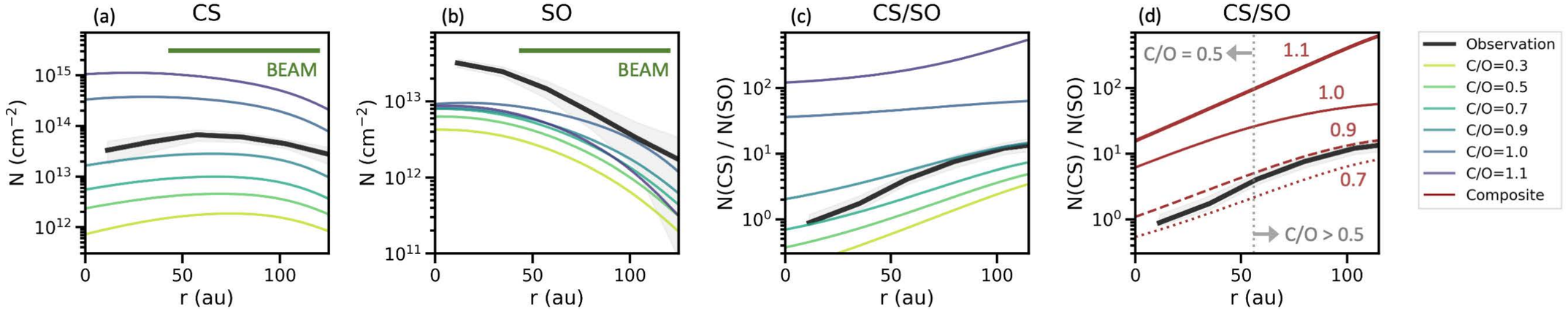

SiS分布：既存の円盤化学モデルでは説明できないほど enhance → Protoplanetへの降着流？

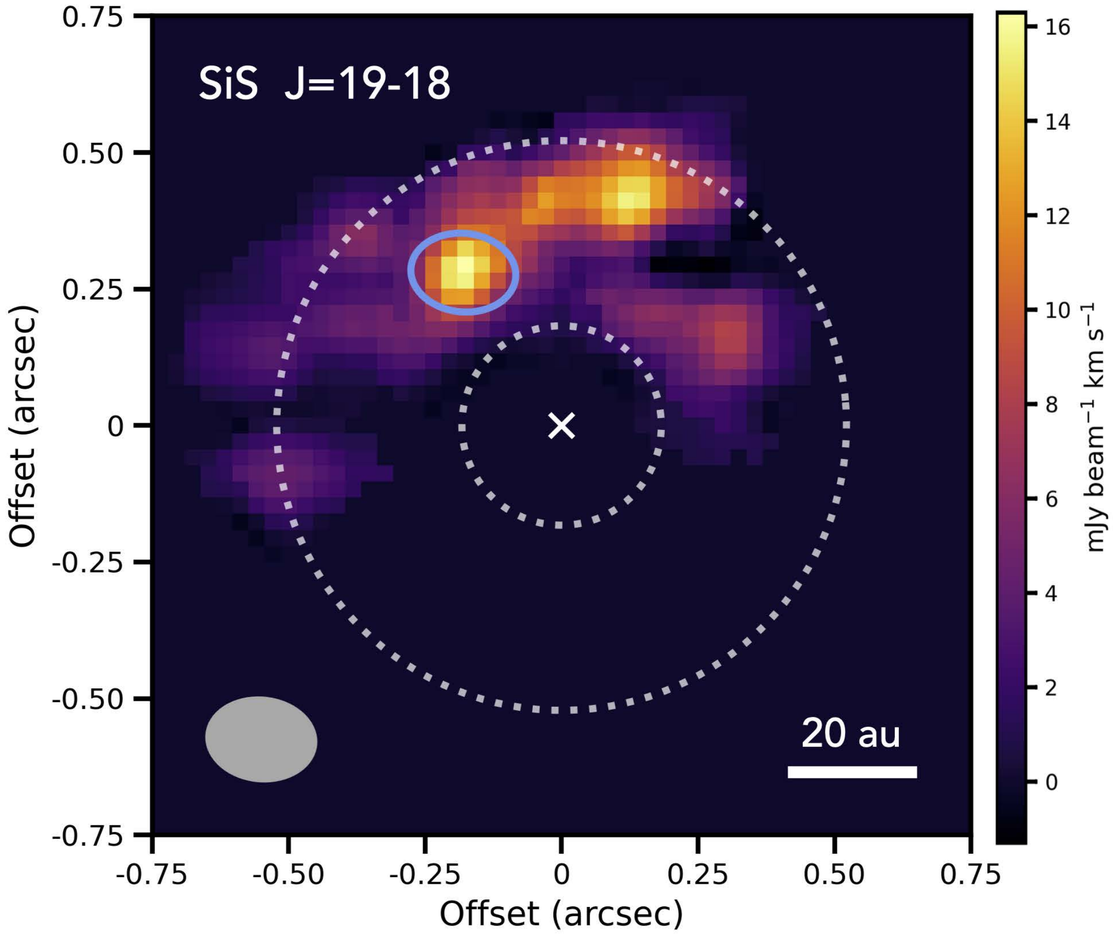

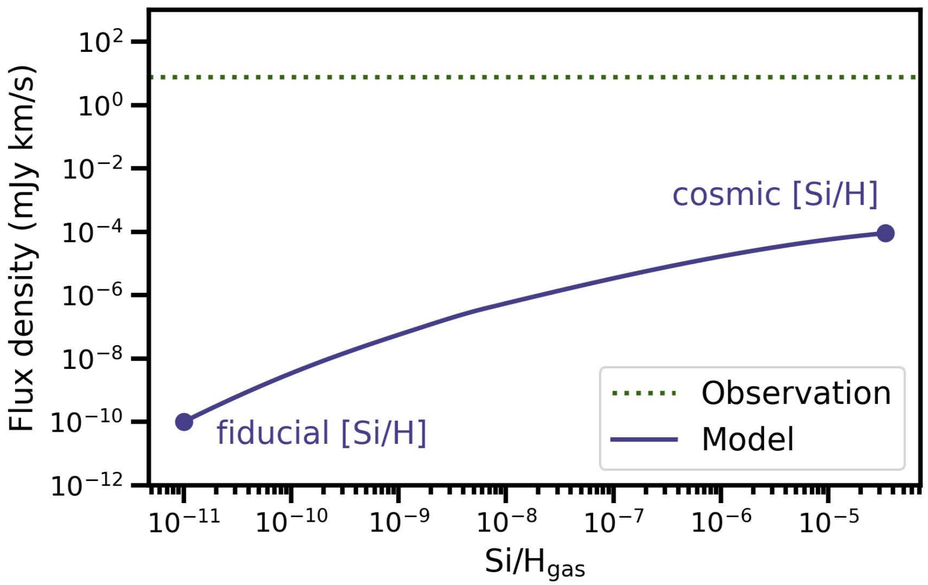

Figure 8. *Top:* SiS $J = 19-18$ integrated intensity map. Dotted white ellipses denote peaks of the dust rings. The light blue ellipse encompasses the area in which the flux density was measured. The beam size is denoted by the solid grey ellipse in the lower left. *Bottom:* Observed vs. modelled SiS $J = 19-18$ flux density, as measured in vicinity of the protoplanet (light blue ellipse in top panel). The models span a range of total elemental Si and S abundances, starting at the fiducial value and increasing up to the cosmic abundance.

Discovery of interstellar 1-cyanopyrene: a four-ring polycyclic aromatic hydrocarbon in TMC-1

Gabi Wenzel, Ilsa R. Cooke, P. Bryan Changala, Edwin A. Bergin, Shuo Zhang et al.

Polycyclic aromatic hydrocarbons (PAHs) are expected to be the most abundant class of organic molecules in space. Their interstellar lifecycle is not well understood, and progress is hampered by difficulties detecting individual PAH molecules. Here, we present the discovery of CN-functionalized pyrene, a 4-ring PAH, in the dense cloud TMC-1 using the 100-m Green Bank Telescope. We derive an abundance of 1-cyanopyrene of $\sim 1.52 \times 10^{12}\,\mathrm{cm}^{-2}$, and from this estimate that the un-substituted pyrene accounts for up to $0.03 - 0.3\,\%$ of the carbon budget in the dense interstellar medium which trace the birth sites of stars and planets. The presence of pyrene in this cold ($\sim$10 K) molecular cloud agrees with its recent measurement in asteroid Ryugu where isotopic clumping suggest a cold, interstellar origin. The direct link to the birth site of our solar system is strengthened when we consider the solid state pyrene content in the pre-stellar materials compared to comets, which represent the most pristine material in the solar system. We estimate that solid state pyrene can account for 1 % of the carbon within comets carried by this one single organic molecule. The abundance indicates pyrene is an "island of stability" in interstellar PAH chemistry and suggests a potential cold molecular cloud origin of the carbon carried by PAHs that is supplied to forming planetary systems, including habitable worlds such as our own.

- 4環芳香族であるピレンのシアン化物の1-シアノピレンの回転遷移をTMC-1で検出
- 柱密度の導出，Carbon-budgetの0.03-0.3%を占める
- 固体成分の見積もりも合わせると1%? “Island of stability”
- Ryuguサンプルのピレン同位体分析の結果（冷たい環境起源を示唆）と整合的

Detections of interstellar 2-cyanopyrene and 4-cyanopyrene in TMC-1

Gabi Wenzel, Thomas H. Speak, P. Bryan Changala, Reace H. J. Willis, Andrew M. Burkhardt et al.

Abstract

Polycyclic aromatic hydrocarbons (PAHs) are among the most ubiquitous compounds in the universe, accounting for up to ∼25 % of all interstellar carbon. Since most unsubstituted PAHs do not possess permanent dipole moments, they are invisible to radio astronomy. Constraining their abundances relies on the detection of polar chemical proxies, such as aromatic nitriles. We report the detection of 2- and 4-cyanopyrene, isomers of the recently detected 1-cyanopyrene. We find that these isomers are present in an abundance ratio of ∼2:1:2, which mirrors the number of equivalent sites available for CN addition. We conclude that there is evidence that the cyanopyrene isomers formed by direct CN addition to pyrene under kinetic control in hydrogen-rich gas at 10 K and discuss constraints on the H:CN ratio for PAHs in TMC-1.

Keywords: interstellar medium, polycyclic aromatic hydrocarbons, molecular clouds, astrochemistry

- シアノピレンの異性体（2-シアノピレン, 4-シアノピレン）回転遷移をTMC-1で検出
- 柱密度の導出，異性体間の存在比はCNの同等な位置の割合と合致，低温環境下での速度論的制御のもとでCNのダイレクトな付加で生成
- PAHs中のH:CNやPAHsの生成機構についても議論

ピレンとシアノピレン

$C_{16}H_{10}$

PAHの基本的なユニットの1つ

対称分子なので回転遷移検出困難

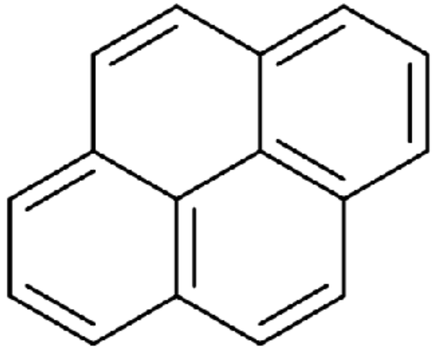

1-シアノピレン

Hの代わりにCNがくっつく

回転遷移が検出可能に

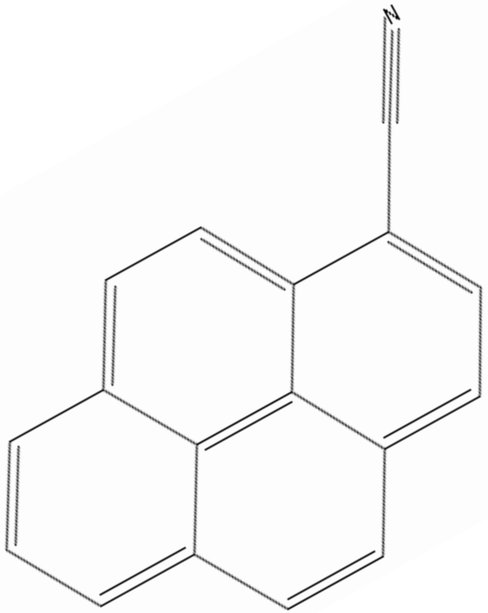

2-シアノピレン，4-シアノピレン

CN基がつく場所で区別

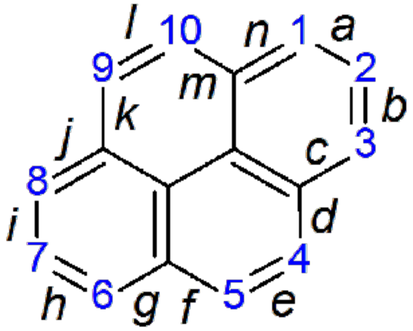

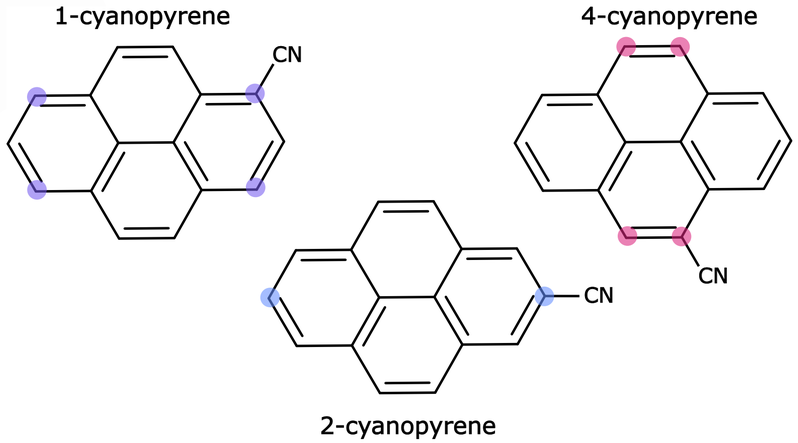

GOTHAM surveyによるcyanopyreneの検出

- The GOTHAM – GBT Observations of TMC-1: Hunting Aromatic Molecules
- Rotational Spectroscopy との組み合わせ

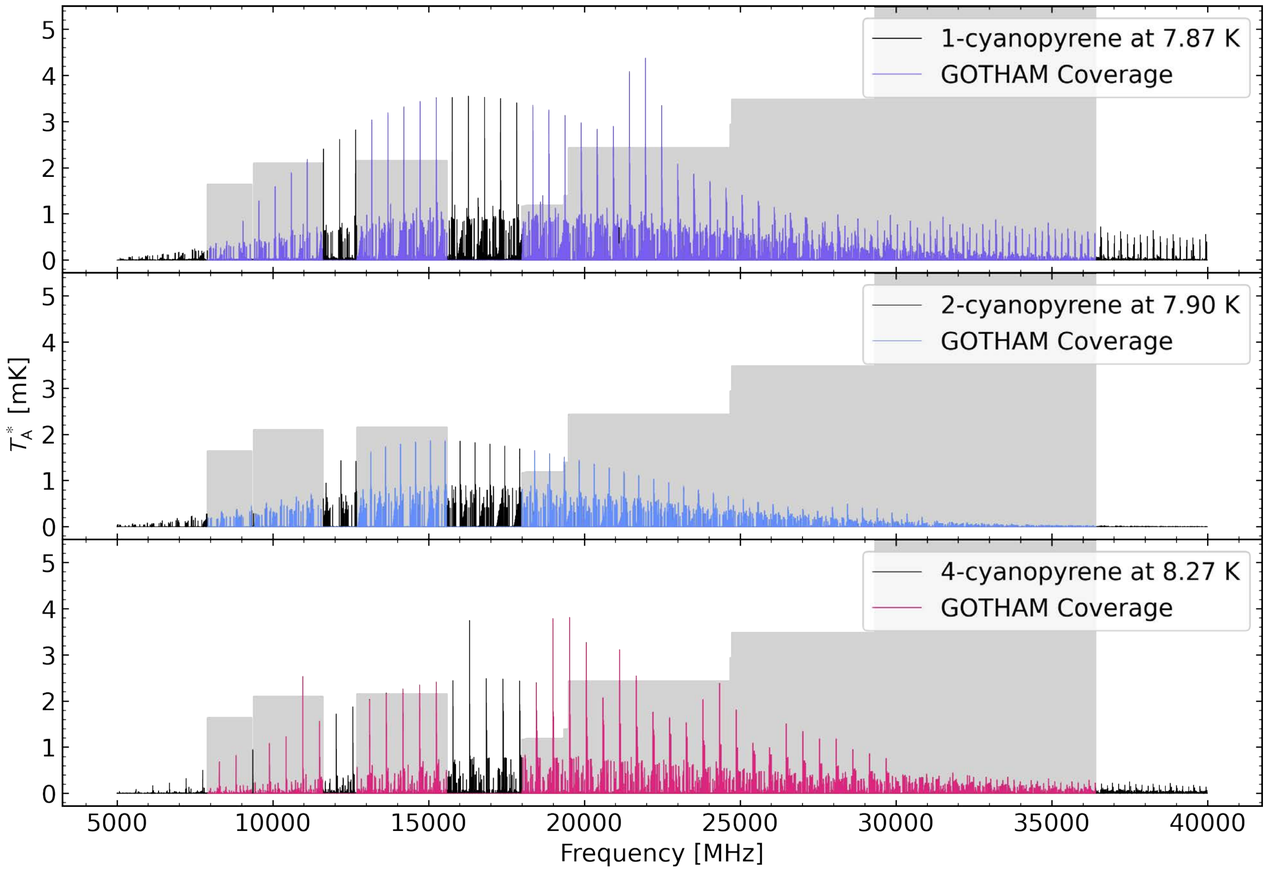

Fig. A1 Frequency coverage of TMC-1 in the GOTHAM data set. Rotational spectra of 1-cyanopyrene (top panel), 2-cyanopyrene (center panel), and 4-cyanopyrene (bottom panel) simulated at the MCMC derived excitation temperatures of 7.87 K, 7.90 K, and 8.27 K, respectively, are depicted in black. The lines that are covered by the GOTHAM data are depicted in color. The grey shaded areas indicate the averaged noise level of the observation in each data chunk.

GOTHAM surveyによる1-cyanopyreneの検出

生スペクトルの例

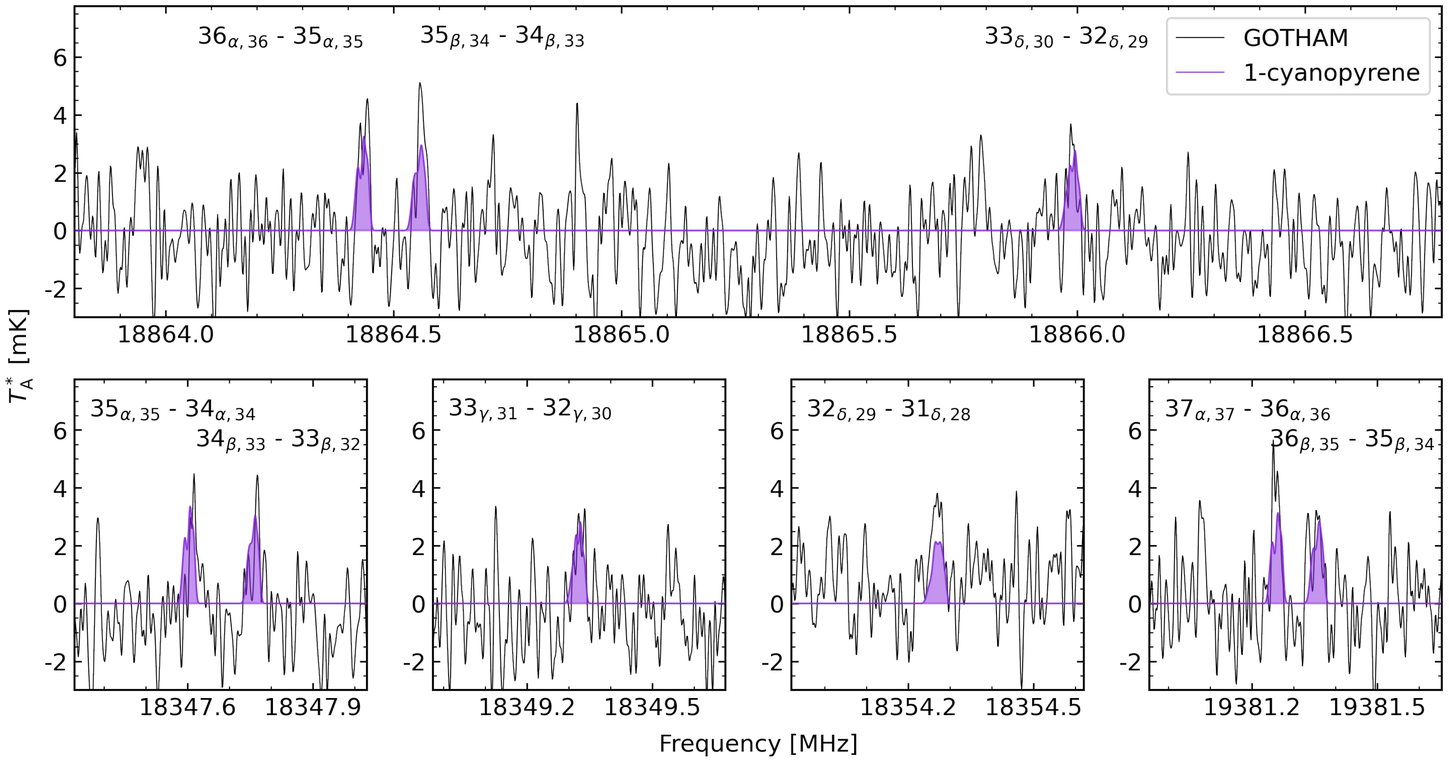

Figure 2: **GOTHAM spectra showcasing several 1-cyanopyrene lines detected in TMC-1 observations.** The original GOTHAM observational data for which one channel corresponds to $1.4\,\mathrm{kHz}$ were smoothed with a Hanning window to a resolution of $14\,\mathrm{kHz}$, depicted in black. The spectrum of 1-cyanopyrene is overplotted in violet using source-dependent molecular parameters as reported in Table S4. The quantum numbers of each transition, ignoring ^{14}N nuclear electric quadrupole splitting, are reported. Each line contains multiple closely spaced K-components of each transition which are denoted $\alpha, \beta, \gamma, \delta = \{0,1\}, \{1,2\}, \{2,3\}, \{3,4\}$.

GOTHAM surveyによる1-cyanopyreneの検出

速度軸で揃えた
スタッキング

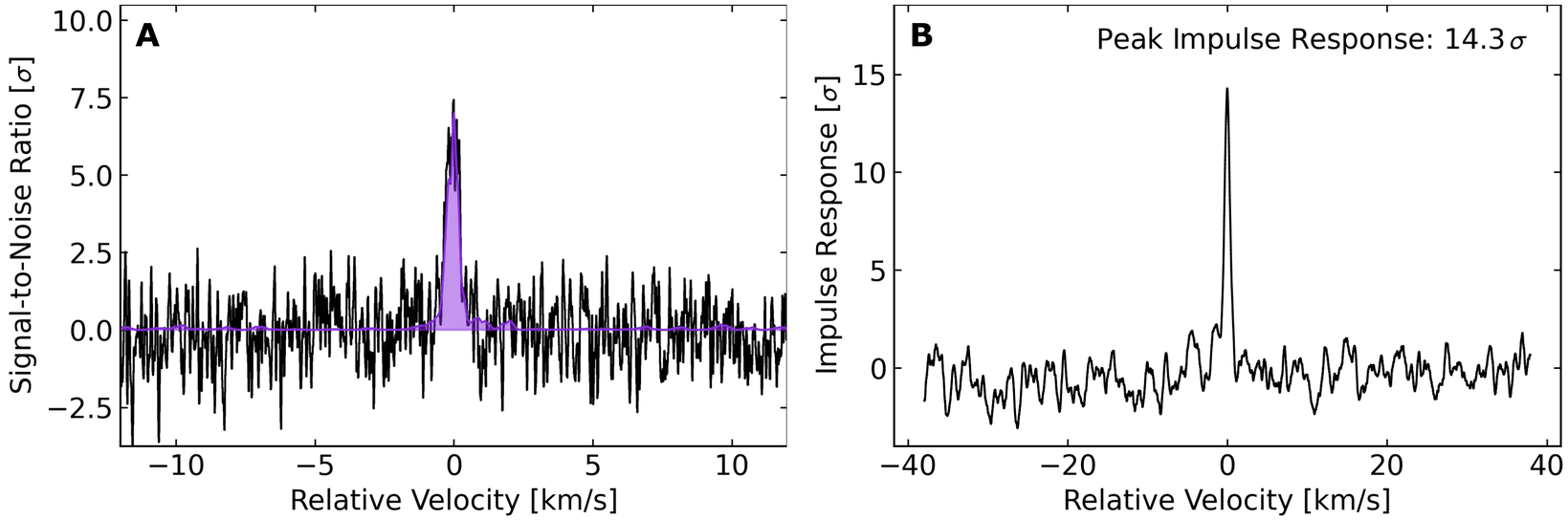

Figure 3: **Velocity-stacked spectra and matched filter response of 1-cyanopyrene.** The stacked GOTHAM observations (black) are overlaid with the 1-cyanopyrene stacked spectrum (violet) for the 150 brightest SNR 1-cyanopyrene lines (**A**). The corresponding impulse response for the matched filtering analysis is shown yielding a significance of $14.3\,\sigma$ for the 1-cyanopyrene detection (**B**).

2-cyanopyrene, 4-cyanopyreneの検出

速度軸で揃えた
スタッキング

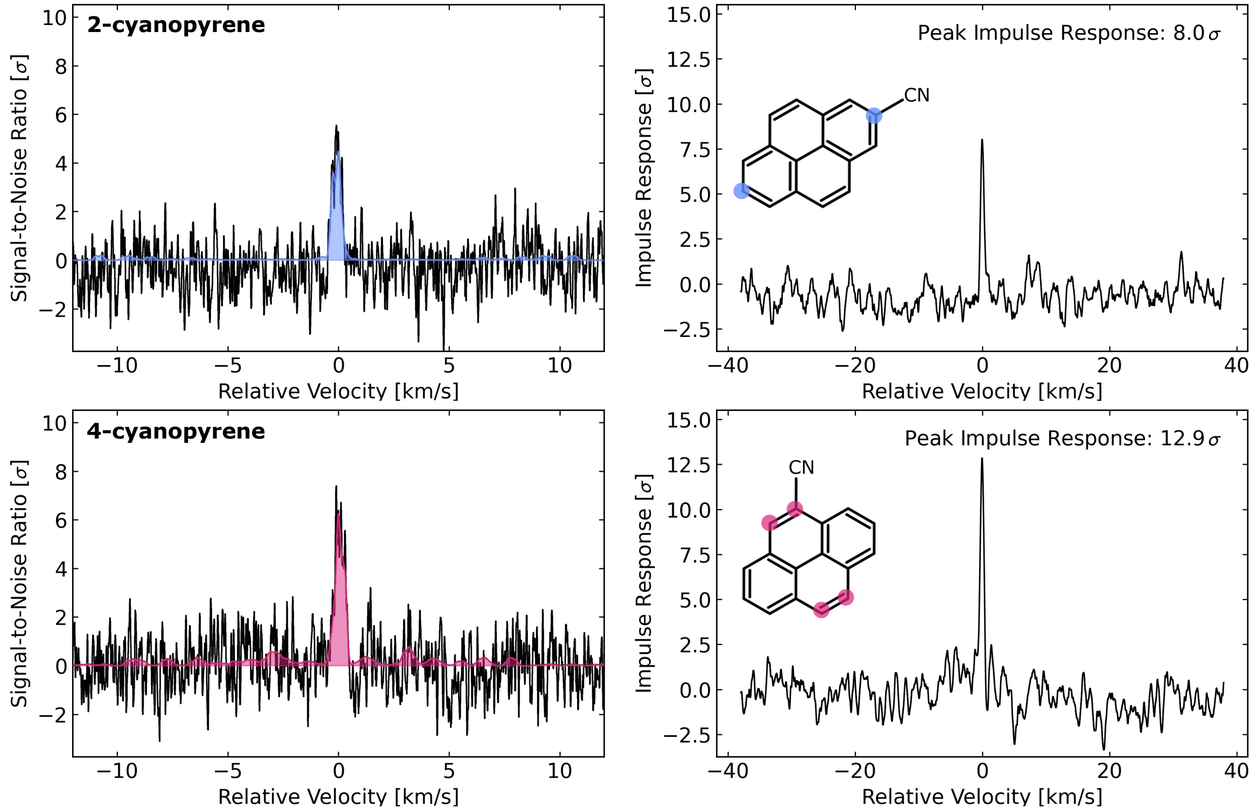

Fig. 2 Velocity-stacked spectra and matched filter responses of 2- and 4-cyanopyrene. The stacked GOTHAM observations (black) are overlaid with the simulated stacked spectrum of 2- and 4-cyanopyrene (blue and pink, respectively), each consisting of the 150 brightest SNR lines (left panels). Marginalized posterior parameters were used in both simulations, as reported in Supplementary Table A3. The corresponding impulse response for the matched filtering analysis is shown, yielding a significance of $8.0\,\sigma$ and $12.9\,\sigma$ for the 2- and 4-cyanopyrene detections, respectively (right panels). The small features in the stacked simulated spectrum (pink) in the bottom left panel result from the densely populated 4-cyanopyrene lines (see Fig. A3) that add up in the stack.

MCMCによる柱密度の導出

Table A3 MCMC fit parameters for 1-cyanopyrene as reported in ref. [21], and 2- and 4-cyanopyrene (this work) using the priors reported in Supplementary Table A2.

1-cyanopyrene

Component No.	$v_{\rm lsr}$ [km s^{-1}]	Size [″]	N_T [10^{11} cm^{-2}]	$T_{\rm ex}$ [K]	ΔV [km s^{-1}]
1	$5.603^{+0.012}_{-0.012}$	50	$4.15^{+0.62}_{-0.59}$	$7.87^{+0.43}_{-0.40}$	$0.150^{+0.016}_{-0.013}$
2	$5.747^{+0.010}_{-0.011}$	50	$5.81^{+0.68}_{-0.61}$		
3	$5.930^{+0.016}_{-0.026}$	49	$3.75^{+0.70}_{-1.21}$		
4	$6.036^{+0.046}_{-0.042}$	49	$1.49^{+1.38}_{-0.71}$		
N_T(Total) : $1.52^{+0.18}_{-0.16} \times 10^{12}$ cm^{-2}					

2-cyanopyrene

Component No.	$v_{\rm lsr}$ [km s^{-1}]	Size [″]	N_T [10^{11} cm^{-2}]	$T_{\rm ex}$ [K]	ΔV [km s^{-1}]
1	$5.603^{+0.005}_{-0.005}$	49	$0.78^{+0.36}_{-0.30}$	$7.90^{+0.53}_{-0.48}$	$0.191^{+0.018}_{-0.019}$
2	$5.751^{+0.005}_{-0.005}$	49	$3.52^{+0.52}_{-0.46}$		
3	$5.928^{+0.005}_{-0.005}$	50	$1.60^{+0.48}_{-0.51}$		
4	$6.038^{+0.005}_{-0.005}$	50	$2.51^{+0.50}_{-0.44}$		
N_T(Total) : $8.41^{+0.94}_{-0.87} \times 10^{11}$ cm^{-2}					

4-cyanopyrene

Component No.	$v_{\rm lsr}$ [km s^{-1}]	Size [″]	N_T [10^{11} cm^{-2}]	$T_{\rm ex}$ [K]	ΔV [km s^{-1}]
1	$5.601^{+0.005}_{-0.004}$	50	$3.94^{+0.46}_{-0.42}$	$8.27^{+0.46}_{-0.44}$	$0.179^{+0.016}_{-0.015}$
2	$5.752^{+0.005}_{-0.005}$	50	$3.49^{+0.53}_{-0.51}$		
3	$5.925^{+0.005}_{-0.005}$	50	$5.20^{+0.62}_{-0.56}$		
4	$6.036^{+0.005}_{-0.005}$	50	$0.66^{+0.41}_{-0.25}$		
N_T(Total) : $1.33^{+0.10}_{-0.09} \times 10^{12}$ cm^{-2}					

2-cyanopyreneの場合

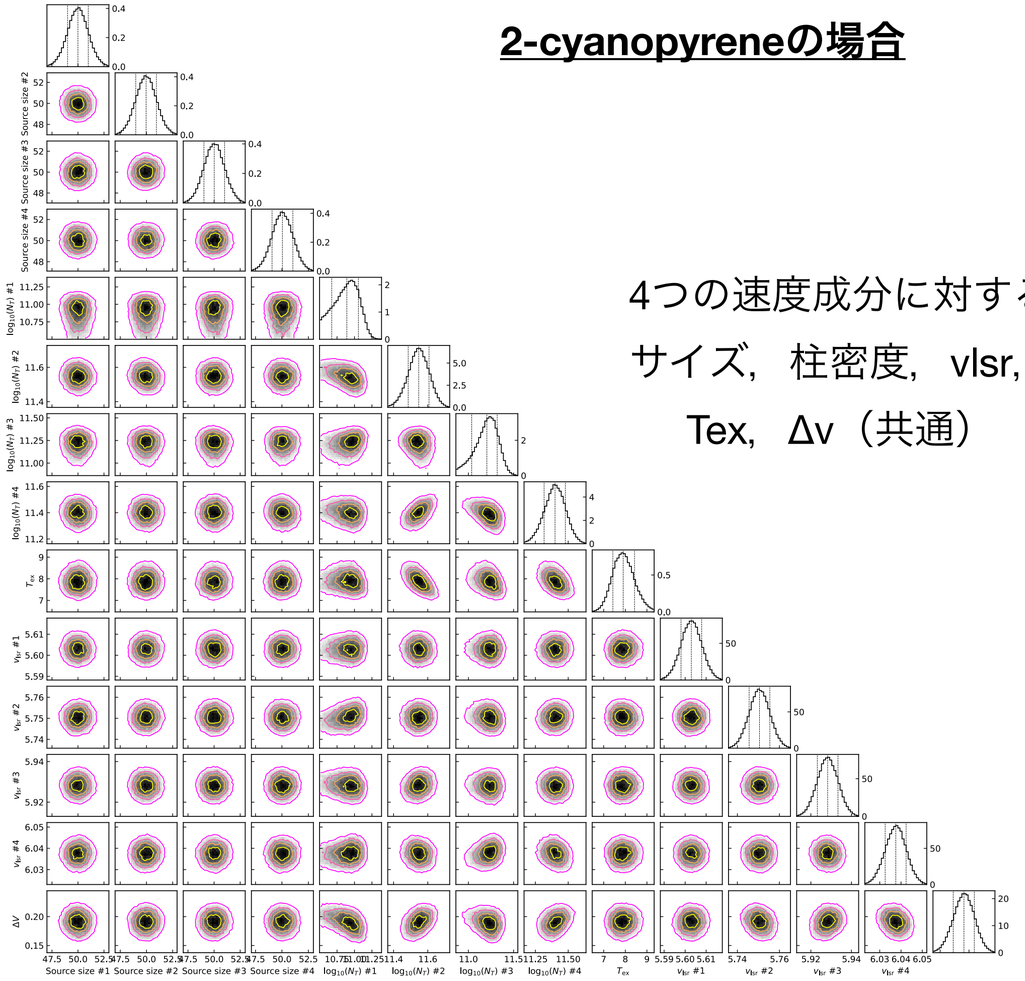

4つの速度成分に対する
サイズ，柱密度，vlsr，
Tex，Δv（共通）

Fig. A4 Corner plot of MCMC analysis for 2-cyanopyrene. This shows the parameter covariances on the off-diagonal and marginalized posterior distributions considered in the marginalized posterior distributions on-diagonal. The $16^{\rm th}$, $50^{\rm th}$, and $84^{\rm th}$ confidence intervals (corresponding to $\pm 1\,\sigma$ for a Gaussian posterior distribution) are shown as vertical lines on the diagonal.

MCMCによる柱密度の導出

Table A3 MCMC fit parameters for 1-cyanopyrene as reported in ref. [21], and 2- and 4-cyanopyrene (this work) using the priors reported in Supplementary Table A2.

1-cyanopyrene

Component No.	$v_{\rm lsr}$ [km s^{-1}]	Size [″]	N_T [10^{11} cm^{-2}]	$T_{\rm ex}$ [K]	ΔV [km s^{-1}]
1	$5.603^{+0.012}_{-0.012}$	50	$4.15^{+0.62}_{-0.59}$	$7.87^{+0.43}_{-0.40}$	$0.150^{+0.016}_{-0.013}$
2	$5.747^{+0.010}_{-0.011}$	50	$5.81^{+0.68}_{-0.61}$		
3	$5.930^{+0.016}_{-0.026}$	49	$3.75^{+0.70}_{-1.21}$		
4	$6.036^{+0.046}_{-0.042}$	49	$1.49^{+1.38}_{-0.71}$		
N_T(Total) : $1.52^{+0.18}_{-0.16} \times 10^{12}$ cm^{-2}					

2-cyanopyrene

Component No.	$v_{\rm lsr}$ [km s^{-1}]	Size [″]	N_T [10^{11} cm^{-2}]	$T_{\rm ex}$ [K]	ΔV [km s^{-1}]
1	$5.603^{+0.005}_{-0.005}$	49	$0.78^{+0.36}_{-0.30}$	$7.90^{+0.53}_{-0.48}$	$0.191^{+0.018}_{-0.019}$
2	$5.751^{+0.005}_{-0.005}$	49	$3.52^{+0.52}_{-0.46}$		
3	$5.928^{+0.005}_{-0.005}$	50	$1.60^{+0.48}_{-0.51}$		
4	$6.038^{+0.005}_{-0.005}$	50	$2.51^{+0.50}_{-0.44}$		
N_T(Total) : $8.41^{+0.94}_{-0.87} \times 10^{11}$ cm^{-2}					

4-cyanopyrene

Component No.	$v_{\rm lsr}$ [km s^{-1}]	Size [″]	N_T [10^{11} cm^{-2}]	$T_{\rm ex}$ [K]	ΔV [km s^{-1}]
1	$5.601^{+0.005}_{-0.004}$	50	$3.94^{+0.46}_{-0.42}$	$8.27^{+0.46}_{-0.44}$	$0.179^{+0.016}_{-0.015}$
2	$5.752^{+0.005}_{-0.005}$	50	$3.49^{+0.53}_{-0.51}$		
3	$5.925^{+0.005}_{-0.005}$	50	$5.20^{+0.62}_{-0.56}$		
4	$6.036^{+0.005}_{-0.005}$	50	$0.66^{+0.41}_{-0.25}$		
N_T(Total) : $1.33^{+0.10}_{-0.09} \times 10^{12}$ cm^{-2}					

- 1-cyanopyrene の柱密度 1.5×10^{12} cm^{-2}
  - Hに対する存在度は1.5×10^{-10}！
- Pure vs. CN-substituted = H:CN ratioは(10-100):1（次ページ：他の関連分子の値から→ pyreneの存在度は(0.15-1.5) × 10^{-8}と推定。これはcarbon budgetの0.03-0.3%に当たる。
- 柱密度の比が2:1:2。同等なC原子の場所の数に比例→低温環境下での速度論的制御のもとでCNのダイレクトな付加で生成

H:CNの見積もりとC budget

Table S5: Column densities of select carbon-bearing molecules observed in TMC-1. The abundance of carbon in each molecule (f_C) in ppm is found by multiplying the abundance, n(X)/n(H), with the number of carbons in the molecule (N_C). Unfunctionalized hydrocarbons are shown in bold.

Molecule	N_C	Column Density $[10^{12}\ \mathrm{cm}^{-2}]$	f_C [ppm]	Reference
C_5H_6	5	12^{+3}_{-3}	6×10^{-3}	(*23*)
1-C_5H_5CN	6	$0.827^{+0.09}_{-0.10}$	5×10^{-4}	(*68*)
2-C_5H_5CN	6	$0.189^{+0.018}_{-0.015}$	1×10^{-4}	(*68*)
C_6H_5CN	7	$1.73^{+0.85}_{-0.10}$	1×10^{-3}	(*21*)
C_9H_8	9	$9.04^{+0.96}_{-0.96}$	8×10^{-3}	(*24*)
2-C_9H_7CN	10	$0.210^{+0.060}_{-0.046}$	2×10^{-4}	(*24*)
1-$C_{10}H_7CN$	11	$0.735^{+0.330}_{-0.463}$	8×10^{-4}	(*21*)
2-$C_{10}H_7CN$	11	$0.705^{+0.450}_{-0.323}$	8×10^{-4}	(*21*)
1-$C_{16}H_9CN$	17	$1.52^{+0.18}_{-0.16}$	3×10^{-3}	This work
$C_{16}H_{10}$*	16	15–150	$2\ (\times 10^{-2} - 10^{-1})$	This work

* estimated using the 1-cyanopyrene abundance and taking a H:CN ratio of 10:1 – 100:1.

The observed H:CN ratios
14.5:1 (C_5H_6:1-C_5H_5CN), 43:1 (C_9H_8:2-C_9H_7CN) and 63:1 (C_5H_6:2-C_5H_5CN).

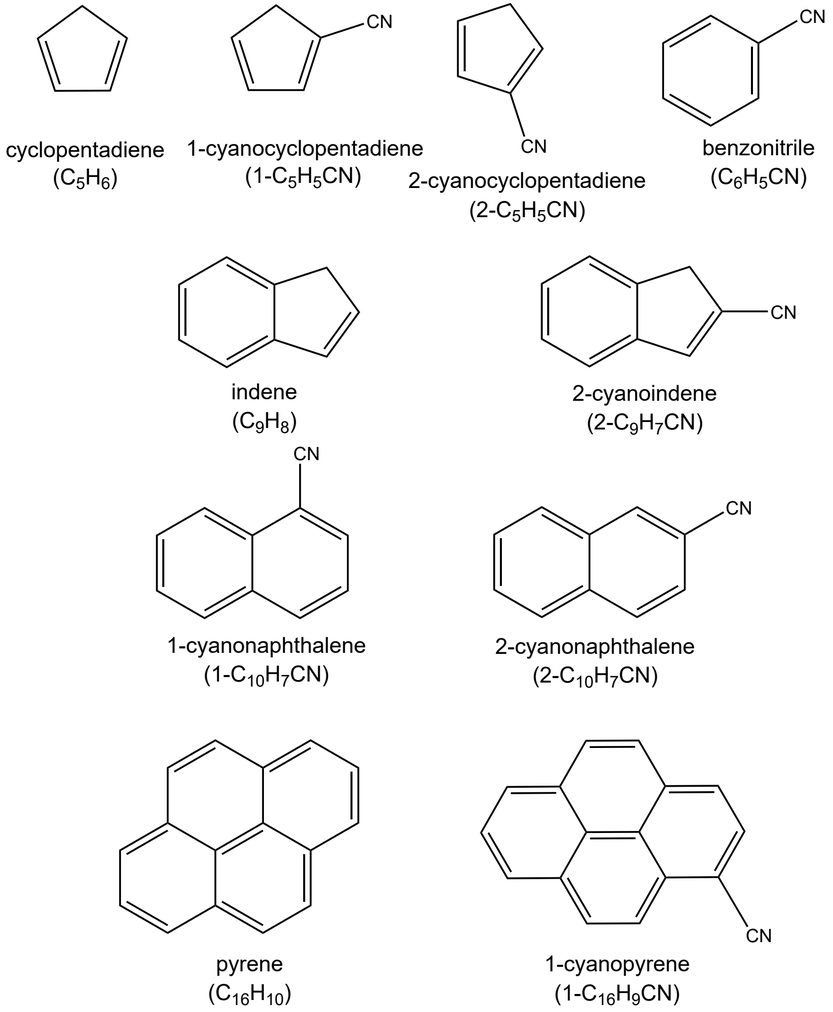

MCMCによる柱密度の導出

Table A3 MCMC fit parameters for 1-cyanopyrene as reported in ref. [21], and 2- and 4-cyanopyrene (this work) using the priors reported in Supplementary Table A2.

1-cyanopyrene

Component No.	$v_{\rm lsr}$ [km s^{-1}]	Size [″]	N_T [10^{11} cm^{-2}]	$T_{\rm ex}$ [K]	ΔV [km s^{-1}]
1	$5.603^{+0.012}_{-0.012}$	50	$4.15^{+0.62}_{-0.59}$	$7.87^{+0.43}_{-0.40}$	$0.150^{+0.016}_{-0.013}$
2	$5.747^{+0.010}_{-0.011}$	50	$5.81^{+0.68}_{-0.61}$		
3	$5.930^{+0.016}_{-0.026}$	49	$3.75^{+0.70}_{-1.21}$		
4	$6.036^{+0.046}_{-0.042}$	49	$1.49^{+1.38}_{-0.71}$		
N_T(Total) : $1.52^{+0.18}_{-0.16} \times 10^{12}$ cm^{-2}					

2-cyanopyrene

Component No.	$v_{\rm lsr}$ [km s^{-1}]	Size [″]	N_T [10^{11} cm^{-2}]	$T_{\rm ex}$ [K]	ΔV [km s^{-1}]
1	$5.603^{+0.005}_{-0.005}$	49	$0.78^{+0.36}_{-0.30}$	$7.90^{+0.53}_{-0.48}$	$0.191^{+0.018}_{-0.019}$
2	$5.751^{+0.005}_{-0.005}$	49	$3.52^{+0.52}_{-0.46}$		
3	$5.928^{+0.005}_{-0.005}$	50	$1.60^{+0.48}_{-0.51}$		
4	$6.038^{+0.005}_{-0.005}$	50	$2.51^{+0.50}_{-0.44}$		
N_T(Total) : $8.41^{+0.94}_{-0.87} \times 10^{11}$ cm^{-2}					

4-cyanopyrene

Component No.	$v_{\rm lsr}$ [km s^{-1}]	Size [″]	N_T [10^{11} cm^{-2}]	$T_{\rm ex}$ [K]	ΔV [km s^{-1}]
1	$5.601^{+0.005}_{-0.004}$	50	$3.94^{+0.46}_{-0.42}$	$8.27^{+0.46}_{-0.44}$	$0.179^{+0.016}_{-0.015}$
2	$5.752^{+0.005}_{-0.005}$	50	$3.49^{+0.53}_{-0.51}$		
3	$5.925^{+0.005}_{-0.005}$	50	$5.20^{+0.62}_{-0.56}$		
4	$6.036^{+0.005}_{-0.005}$	50	$0.66^{+0.41}_{-0.25}$		
N_T(Total) : $1.33^{+0.10}_{-0.09} \times 10^{12}$ cm^{-2}					

- 1-cyanopyrene の柱密度 1.5×10^{12} cm^{-2}
  - Hに対する存在度は1.5×10^{-10}！
- Pure vs. CN-substituted = H:CN ratioは(10-100):1（次ページ：他の関連分子の値から→ pyreneの存在度は(0.15-1.5) × 10^{-8}と推定。これはcarbon budgetの0.03-0.3%に当たる。
- 柱密度の比が2:1:2。同等なC原子の場所の数に比例→低温環境下での速度論的制御のもとでCNのダイレクトな付加で生成

PAHのformation pathwaysの諸問題

- 高温環境生成 vs. 低温環境生成
  - 低温 ISMに4環芳香族が豊富に存在
  - 太陽系内試料分析：^{13}C置換体からの示唆
    - Ryuguサンプル中の2環と4環PAHs (ナフタレン, フルオランテン, ピレン)は低温星間環境生成?
    - マーチソン隕石の3環PAHs(フェナントレン, アントラセン）やピレンは高温環境下での生成を示唆：星周エンベロープでの形成 or 母天体における変換？
- Bottom-up vs. Top-down

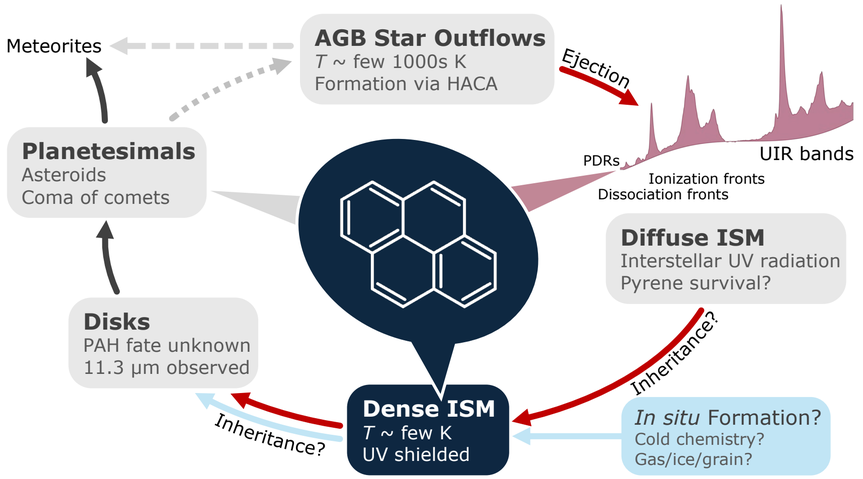

Figure 4: **Ubiquitous presence of PAHs closely connected to the star and cosmic dust lifecycles.** After PAHs are formed in circumstellar envelopes of AGB stars (*19, 53*), they are ejected and seed the diffuse ISM. Here, PAHs are photoprocessed by the interaction with ultraviolet (UV) photons of the interstellar radiation field, which models have shown efficiently destroys PAHs with fewer than 50 carbon atoms (*54*). These astronomical objects are also sources of strong UIR emission (*7*). While we detect 1-cyanopyrene in the cold, dense ISM as a proxy for the radio astronomically invisible pyrene, we cannot explain its high relative abundance through current inheritance or bottom-up formation mechanisms. This necessitates the exploration of possible *in situ* formation routes at low temperatures. Recently, evidence for PAH emission at 11.3 μm has been found in a low-mass protoplanetary disk (*55*), from which finally planetesimals form. Identification of PAHs in carbonaceous chondrites, asteroids, and comets concludes the evidence of the ubiquitous presence of PAHs throughout the ISM.

JWST imaging of edge-on protoplanetary disks
III. Drastic morphological transformation across the mid-infrared in Oph163131

Marion Villenave, Karl R. Stapelfeldt, Gaspard Duchˆene, Franc¸ois M´enard, Marshall D. et al.

ABSTRACT

We present JWST broadband images of the highly inclined protoplanetary disk SSTc2d J163131.2-242627 (Oph163131) from 2.0 to 21μm. The images show a remarkable evolution in disk structure with wavelength, quite different from previous JWST observations of other edge-on disks. At 2.0 and 4.4μm, Oph163131 shows two scattering surfaces separated by a dark lane, typical of highly inclined disks. Starting at 7.7μm however, 1) the two linear nebulosities flanking the dark lane disappear; 2) the brighter nebula tracing the disk upper surface transitions into a compact central source distinctly larger than the JWST PSF and whose intrinsic size increases with wavelength; and 3) patches of extended emission appear at low latitudes, and at surprisingly large radii nearly twice that of the scattered light seen with *HST* and NIRCam, and of the gas. We interpret the compact central source as thermal emission from the star and the inner disk that is not seen directly, but which instead is able to progressively propagate to greater distances at longer wavelengths. The lack of sharp-edged structures in the extended patchy emission argues against the presence of shocks and suggests photoexcitation or stochastic heating of material smoothly flowing away from the star along the disk surface. Finally, the dark lane thickness decreases significantly between 0.6μm and 4.4μm which indicates that the surface layers of Oph163131 lack grains larger than 1μm.

- Edge-on disk Oph163131 のJWSTを使った多波長撮像（+HSTデータ）
- 2.0-4.4umでは，ダークレーンで区切られた2つの散乱表面あり。ダークレーンの厚みは波長が長くなるほど薄くなる。上空には小さなダストのみ存在として再現
- 7.7umで突如，形状が変わる：外側円盤が光学的に薄くなり内側のコンパクトな成分が見え始めることで良く再現

観測結果

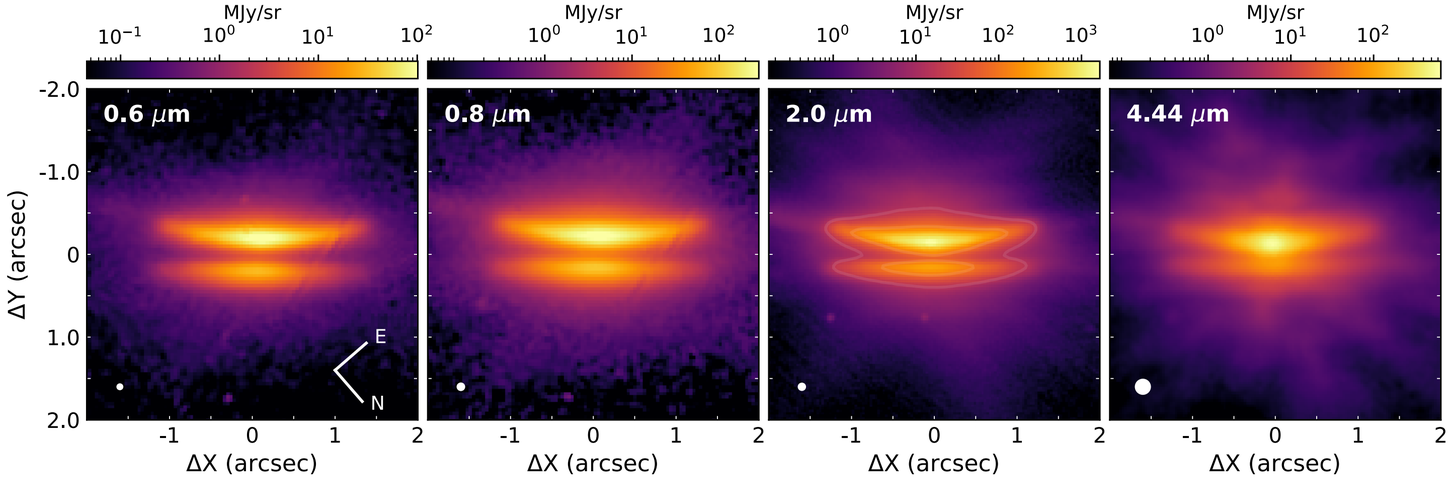

Figure 1. HST/ACS (0.6μm, 0.8μm) and JWST/NIRCam (2.0μm, 4.44μm) images of Oph163131, rotated so that the brighter South-East nebula is up. The white ellipse in the bottom left of each panel represents the resolution of the observations. On the third panel, the faint white contours correspond to 15 MJy/sr and 100 MJy/sr levels in the 2.0μm NIRCam image.

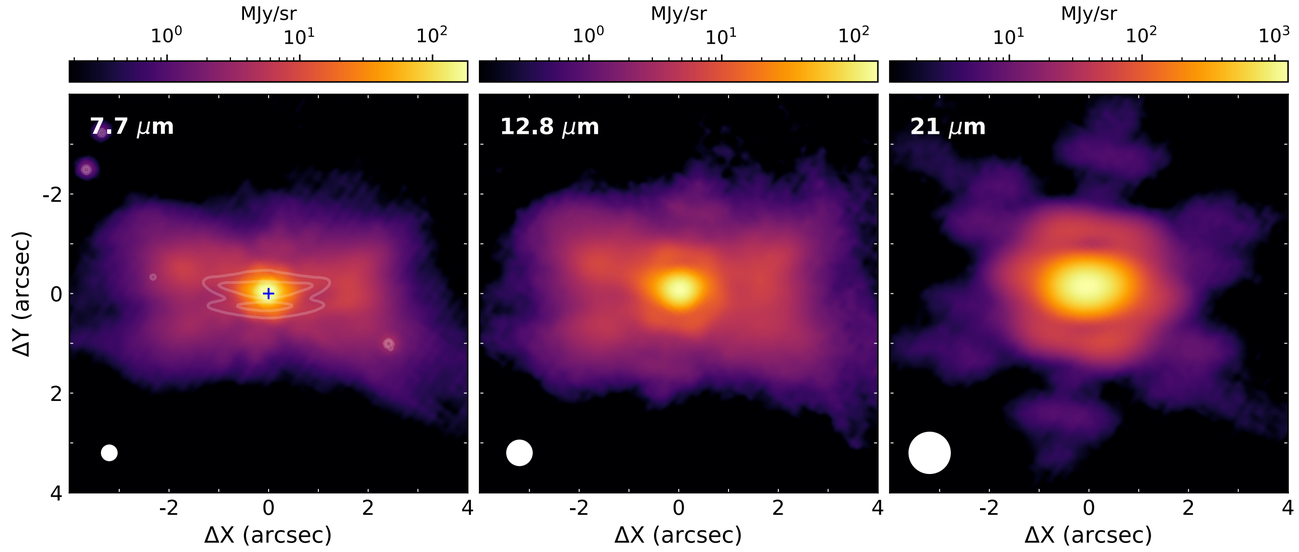

Figure 2. JWST/MIRI images of Oph163131. While the orientation is the same as in Fig. 1, the field of view is twice as large. On the leftmost panel, the white contours correspond to 15 MJy/sr and 100 MJy/sr levels in the 2.0μm NIRCam image (same as in Fig. 1), and the dark cross shows the location of the brightest pixel at 7.7μm. The resolution of the observations is shown as white ellipses in the bottom left corner.

短波長側と長波長側の分布の違い

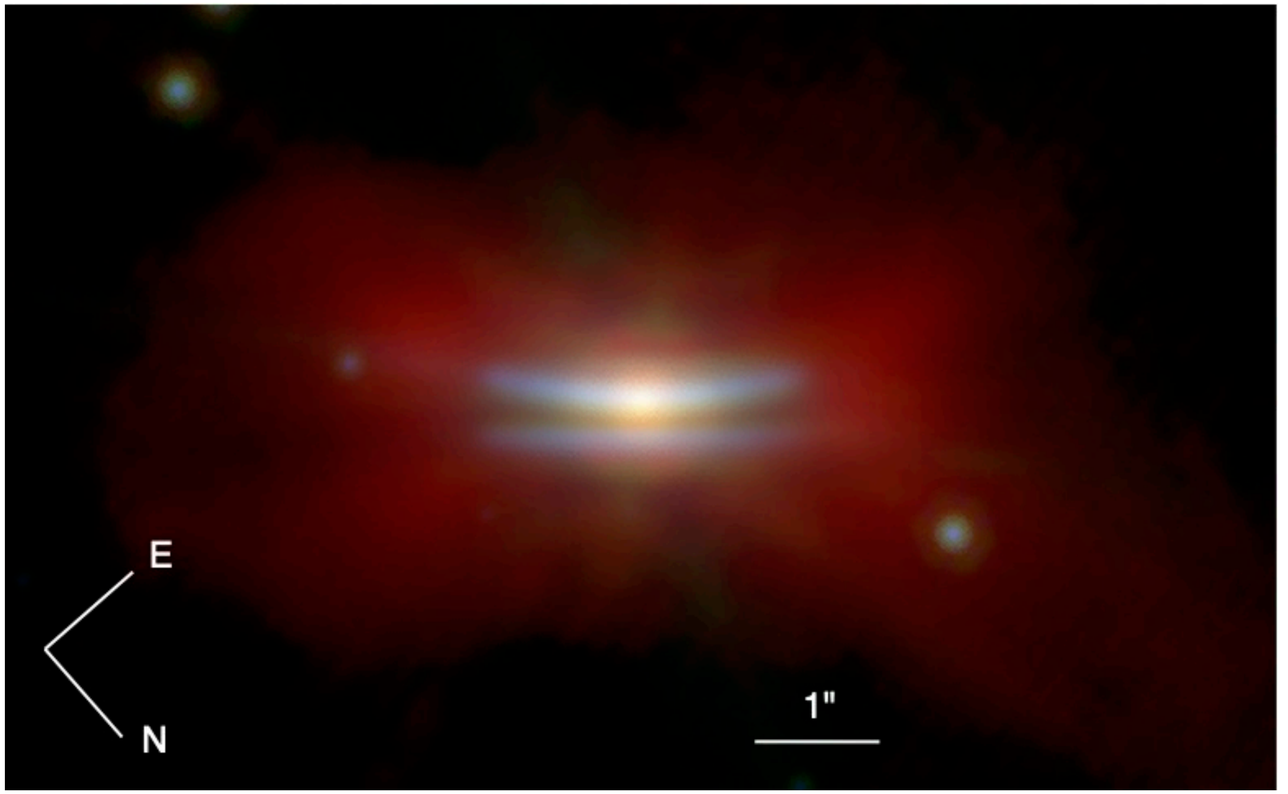

Figure 3. JWST 3-color composite image of Oph163131; the full field of view spans 10×6″. The 2.0, 4.44, and 7.7 μm images are rendered (using a logarithmic stretch) in the blue, green, and red channels, respectively.

短波長側での散乱光・ダークレーンの形態

Table 1. Oph163131 morphological properties

λ (μm)	d_{neb} (")	$\mathrm{FR}_{integrated}$ T/B	R_{FWHM} B (")	R_{FWHM} T (")	$R_{FW10\%}$ B (")	$R_{FW10\%}$ T (")
0.6	0.42 ± 0.01	3.0	0.93 ± 0.11	0.82 ± 0.11	1.88 ± 0.08	1.86 ± 0.05
0.8	0.40 ± 0.01	3.3	0.99 ± 0.12	0.92 ± 0.12	2.00 ± 0.04	1.94 ± 0.04
2.00	0.34 ± 0.01	3.5	1.12 ± 0.10	0.76 ± 0.07	2.17 ± 0.03	1.83 ± 0.07
4.44	0.21 ± 0.01	3.8	0.71 ± 0.07	0.62 ± 0.12	1.84 ± 0.07	1.33 ± 0.08

NOTE—The dark lane thickness (d_{neb}), radial full width half maximum (R_{FWHM}), and the radial full width at 10% of the peak ($R_{10\%}$) are inferred from fitting polynomial spines to the two scattering surfaces. The uncertainties correspond to the statistical error for the different spine averaging. The $\mathrm{FR}_{integrated}$ column instead indicates to the integrated fluxe ratio between both nebula obtained using aperture photometry. We refer to the top (resp. bottom) nebula as "T" (resp. "B").

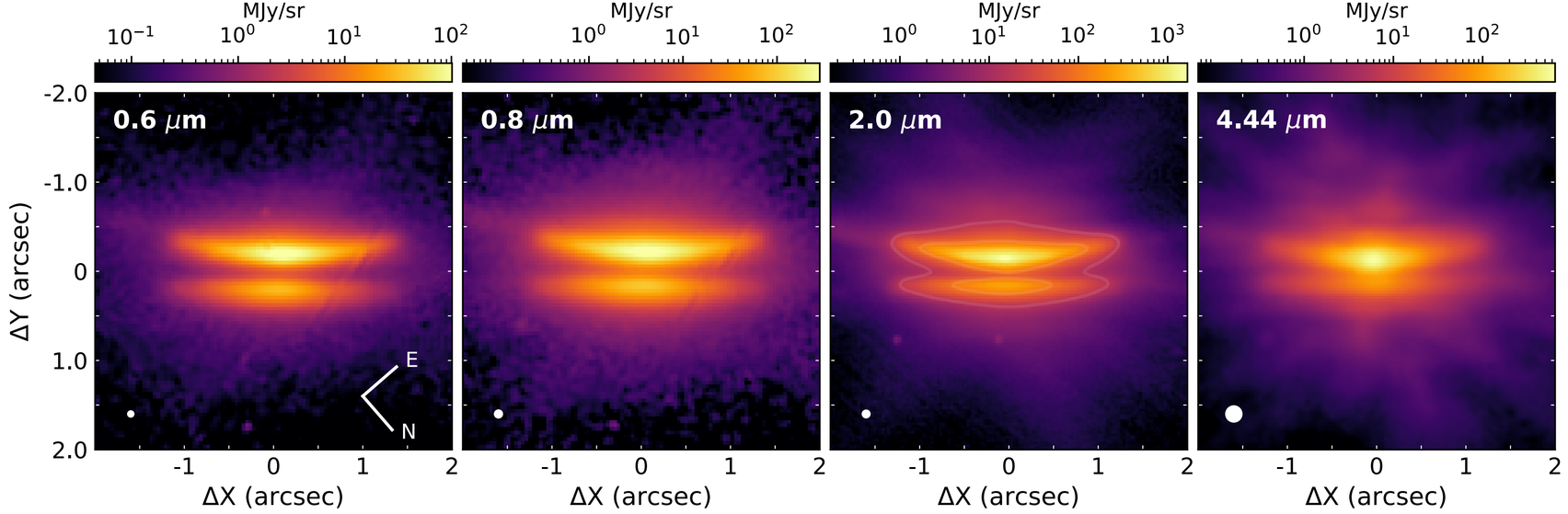

ダークレーンの厚みの波長依存性の再現：ダストサイズ分布を変化させた輻射輸送計算との比較

- 上空に大きなダスト(a≈1mm)が存在するモデルは波長依存性が緩すぎ合わない
- 大きなダストがないか，あっても高度に沈殿していれば定性的に波長依存性を説明可能
- ただし完全に観測を再現できるケースはない
- Edge-on円盤の多様性あり

Table 4. Summary of Model Exploration

Model	Grain Size Distribution			Settling		Total	Dark Lane
	p	$a_{\rm min}$ (μm)	$a_{\rm max}$ (μm)	$\eta_{\rm settl}$	$a_{\rm mix}$ (μm)	Dust Mass ($10^{-4}\,M_\odot$)	Thickness
Standard	3.5	0.03	1000	None		3.94	×
Dust Settling (10)	3.5	0.03	1000	0.5	10	4.59	×
Dust Settling (1)	3.5	0.03	1000	0.5	1	7.10	×
Dust Settling (0.1)	3.5	0.03	1000	0.5	0.1	1400	(✓)
Pristine Dust	3.0	0.03	0.35	None		1.94	(✓)
	1.5	0.35	100				
Only small grains	3.5	0.03	0.5	None		0.43	(✓)

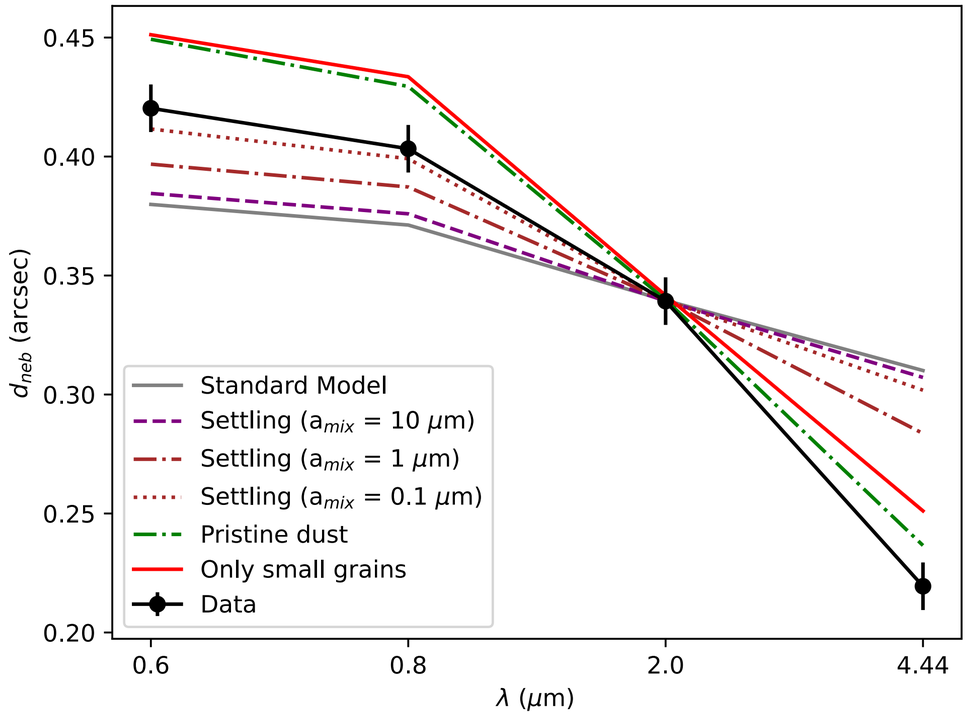

Figure 4. Comparison of data and radiative transfer models of the dark lane thickness as a function of wavelength. The models with grains of 1μm or more present in the upper layers do not show sufficient variation with wavelength to reproduce the observations.

長波長側での中心付近の放射サイズ

Table 2. FWHM of the central source at MIRI wavelengths, along the disk major axis

λ (μm)	Observed ($''$)	*WebbPSF* model ($''$)	Deconvolved ($''$), (au)
7.7	0.44	0.24	0.37, 54
12.8	0.65	0.45	0.47, 70
21.0	1.09	0.71	0.83, 122

PSFより有意に広がり，

長波長側ほどサイズが大きい

中心星の放射ではない

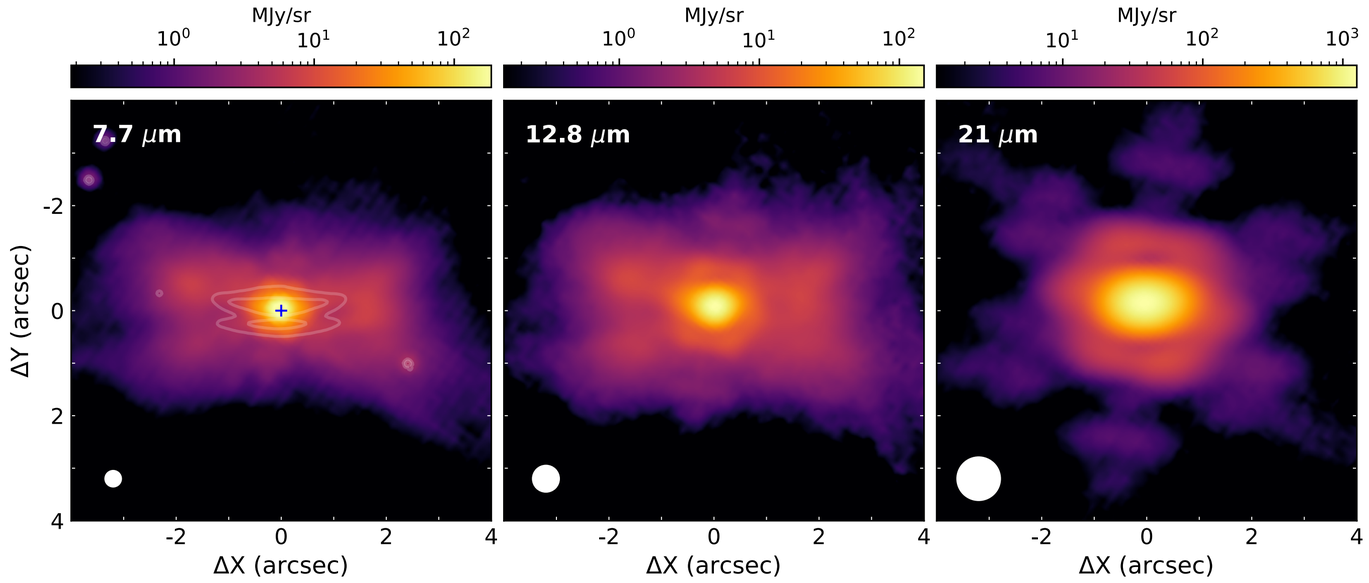

輻射輸送モデルで再現するには中心付近にMassiveで厚みのある構造が必要

中心にmassiveでコンパクトな成分なし

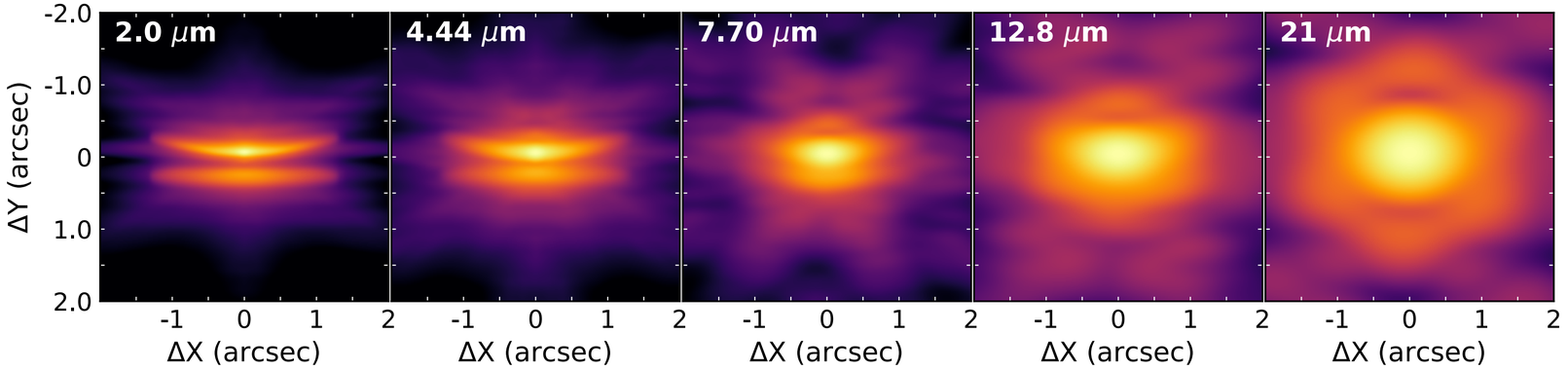

Figure 5. Model A from Wolff et al. (2021), including only one smooth disk region, computed at JWST wavelengths. Contrary to the data, this model does not become dominated by a central source starting at 7.7μm and does not include extended emission at 7.7μm and 12.8μm. The fields of view of the panels 7.7μm, 12.8μm, and 21μm are twice smaller than those in Fig 2.

中心にmassiveでコンパクトな成分あり

短波長側では
外側が光学的に厚く
隠されていたのが
長波長側では光学的に薄く
なり見通せる？

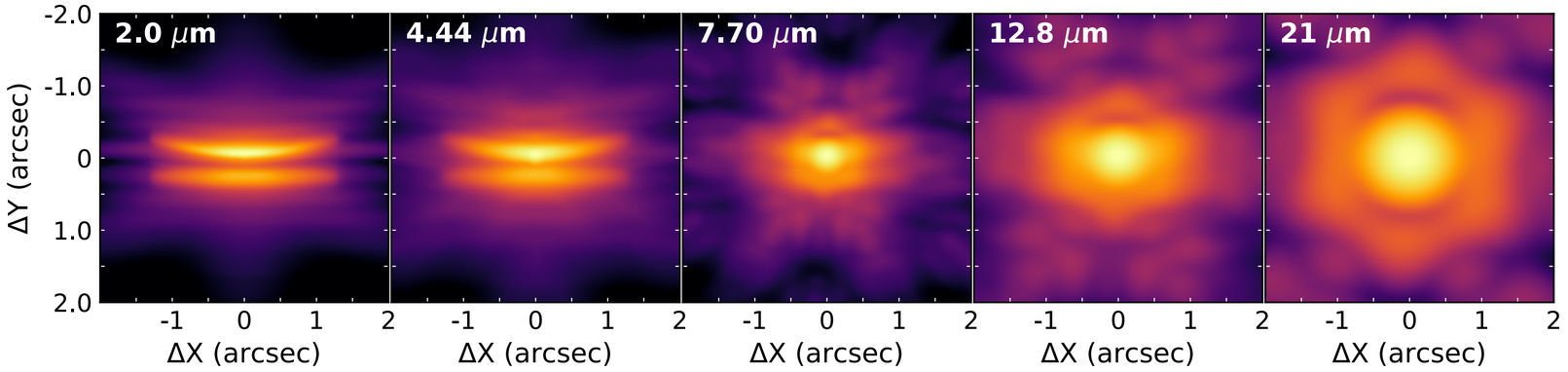

Figure 6. Toy model including a very massive and vertically thick inner region, allowing to reproduce a sharp transition in the source appearance beyond 4.4μm. The fields of view of the panels 7.7μm, 12.8μm, and 21μm are twice smaller than those in Fig 2. The compact source appearing at 7.7μm and longer wavelengths is not centered on the position of the star in the model, but offset by 20mas or more toward the upper nebulae.